The Rydberg Series of Heliumlike Cl, Ar and S and Their High n Satellites in Tokamak Plasmas

J. E. Rice, K. B. Fournier[♭], U. I. Safronova[†] , J. A. Goetz, S. Gutmann[*], A. E. Hubbard, J. Irby, B. LaBombard, E. S. Marmar and J. L. Terry

Plasma Science and Fusion Center, MIT

Cambridge, MA 02139-4307

[♭] *Lawrence Livermore National Laboratory, Livermore, CA 94550*

[*] *Northeastern University, Boston, MA 02116*

[†] *Notre Dame University, Notre Dame, IN 46556*

Abstract

The Rydberg series up to n=14 of heliumlike chlorine, argon and sulphur have been observed in Alcator C-Mod plasmas. High n satellites to these lines of the form $1s^2 2s - 1s2snp$ and $1s^2 2p - 1s2pnp$ with $3 \leq n \leq 12$ have also been seen for chlorine and argon. Accurate wavelengths of these satellites have been obtained, comparison has been made with the theoretical predictions from the atomic structure codes RELAC and MZ, and the agreement is good. Measured line intensities have also been compared with collisional radiative modeling that includes the contributions from dielectronic recombination and inner shell excitation rates to each line's emission, again with good agreement.

I. Introduction

The high n Rydberg series of medium Z heliumlike ions have been observed from Z-pinches [1,2], laser produced plasmas [3], exploding wires [2], the solar corona [4], tokamaks [5-7] and ion traps [8]. Always associated with x-ray emission from these two electron systems are satellite lines from lithiumlike ions. Comparison of observed x-ray spectra with calculated transitions can provide tests of atomic kinetics models and structure calculations for helium- and lithiumlike ions. From wavelength measurements, a systematic study of the n and Z dependence of atomic potentials may be undertaken. From the satellite line intensities, the dynamics of level population by dielectronic recombination and inner shell excitation may be addressed.

Satellites to the Ar^{16+} Rydberg series for n=2 [9,5], n=3 [2,7] and n=4,5 [5,6] have been examined extensively. Theoretical calculations of $n \geq 3$ satellites for argon (and other elements) are plentiful [6,10-13]. For $n \geq 6$ satellites, some wavelengths have been reported [2,5,6], and wavelengths and oscillator strengths have been calculated up to n=7 [1,2], but various wavelength calculations differ from the measured values by 3 mÅ. Observations for Cl^{15+} n=2 transitions have been made in Alcator A [14], Alcator C [15], JET [16] and COMPASS-D [16] plasmas, and n=3 transitions have been seen in laser produced plasmas [3].

The organization of this paper is as follows. The code description and experimental setup are given in Section II. Observations and code comparisons for the Rydberg series of heliumlike Cl^{15+} between n=3 and 14, and the high n satellites of Cl^{14+} with $3 \leq n \leq 10$ are presented in Section III. Similar results for argon are shown in Section IV. The observed Rydberg series of S^{14+} and calculations, including S^{13+} satellites, are given in Section V.

II. Code Descriptions and Experiment

Ab initio atomic structure calculations for the lithium-, helium- and hydro-

genlike isosequences of S, Cl and Ar (Z=16, 17 and 18) with $2 \leq n \leq 14$ have been generated using the HULLAC package. HULLAC includes ANGLAR, which uses the graphical angular recoupling program NJGRAF [17] to generate fine structure levels in a jj-coupling scheme for a set of user-specified electron configurations. HULLAC then generates atomic wavefunctions using the fully relativistic, parametric potential code RELAC [18,19], which calculates the full multi-configuration, intermediate coupled level energies and radiative transition rates. RELAC also computes semi-relativistic autoionization transition rates [20] to the ground and excited levels of an adjacent ion. The CROSS [21] suite of codes in the HULLAC package uses the factorization theorem of Bar-Shalom, Klapisch and Oreg to compute the distorted wave approximation electron-impact excitation rates between all levels of each charge state mentioned above. This includes levels formed by exciting valence shell electrons as well as deeply bound inner shell electrons.

Energy levels and transition probabilities have also been calculated by using the Z-expansion method (MZ code). The energy matrix is constructed in an LSJ coupling scheme and relativistic corrections are included within the framework of the Breit-Pauli operator using a perturbation approach. The MZ method uses hydrogenic wavefunctions. However, the calculation energies and other characteristics by this method are greatly improved by using many-body perturbation theory to include the Coulomb interaction between electrons as well as relativistic corrections. The Z-expansion method has been described in detail in Refs.[22,23].

The ionic transition rates, including the autoionization rates from the Li- to He-like and He-like to H-like ions, as well as direct impact ionization (including ionization from valence and inner shell orbitals) and radiative recombination rate coefficients are used to construct the collisional-radiative rate matrix, $R_{i \rightarrow j}$,

$$\frac{dn_j}{dt} = \sum_i n_i R_{i \rightarrow j} - n_j \sum_i R_{j \rightarrow i} \qquad (1),$$

where n_j is the population in level j, and $R_{i \rightarrow j}$ is the total rate for transitions between level i and j. The inverse of each ionization process, namely dielectronic

recombination and three body recombination has been found according to the principle of detailed balance. The bare nuclei for S, Cl and Ar are also included in the rate matrix; the relative populations of the four charge states are found in the steady state by setting the time derivative of the population in each level equal to zero and inverting the matrix.

The lithiumlike satellite transitions to the heliumlike resonance lines considered here can be excited by two mechanisms, inner shell electron impact excitation of the lithiumlike ion,

$$1s^2 2l + e \rightarrow 1s2lnl' + e \tag{2}$$

or dielectronic recombination from the heliumlike ion,

$$1s^2 + e \rightarrow 1s2lnl^* \rightarrow 1s^2 2l + \gamma \tag{3}$$

where 1s2lnl* is a singly or doubly excited autoionizing lithiumlike level, 1s^{2}2l is a stable lithiumlike level and γ is the observed photon. The emissivity of a line from level j of ion Z excited by electron impact excitation is given by

$$\varepsilon_{\rm Ex} = n_e n_{\rm Z} C_{\rm Ex}(T_e) \beta^R_{j,f} \tag{4}$$

where n_e and $n_{\rm Z}$ are the electron and ion densities, $C_{\rm Ex}(T_e)$ is the impact excitation rate coefficient and $\beta^R_{j,f}$ is the radiative branching ratio for the observed transition from level j to level f. The inner shell excitation channel makes a significant contribution to a lithiumlike satellite line's intensity only when the initial level is the lithiumlike ground level. For the lines in the tables of Sections III and IV that end on excited levels of the lithiumlike ion, the dominant excitation mechanism is via dielectronic recombination.

The emissivity $\varepsilon_{\rm DR}$ of a lithiumlike satellite excited by dielectronic recombination can be expressed as

$$\varepsilon_{\rm DR} = n_e n_{\rm He} F_1(T_e) F_2(j,f) \tag{5},$$

where all the temperature dependence is contained in

$$F_1(T_e) = \left(\frac{4\pi a_0^2 R}{T_e}\right)^{-3/2} exp(-\Delta E_{i,j}/T_e) \qquad (6),$$

where a_0 is the Bohr radius, R is the Rydberg unit of energy and $\Delta E_{i,j}$ is the energy of the captured electron. The satellite intensity factor due to dielectronic recombination from level i of ion (Z+1)+ through level j of ion Z+ to level f is given by

$$F_2(j,f) = \frac{g_j}{g_i} A^A_{j,i} \beta^R_{j,f} \qquad (7),$$

where the gs are the statistical weights of the intermediate (autoionizing) and initial (recombining) levels, $A^A_{j,i}$ is the rate of autoionization from level j to level i, and

$$\beta^R_{j,f} = \frac{A^R_{j,f}}{\Sigma_i A^A_{j,i} + \Sigma_f A^R_{j,f}} \qquad (8)$$

is the branching ratio for radiative stabilization for the observed transition. The sum over i in Eq.(8) runs over all levels in the next higher ion reachable from level j by autoionization, and the sum over f runs over all bound levels reachable from j by radiative decay. Radiative decays from level j to other autoionizing levels have been neglected; stabilization following transitions between continuum levels has a small effect on the computed branching ratio. All atomic data required for Eq.(5) have been generated *ab initio* with RELAC [19,20].

A lithiumlike dielectronic satellite line ($j \rightarrow f$) and the corresponding heliumlike resonance line (w_n) can be used as a temperature diagnostic of the local plasma conditions by dividing Eq.(4) by Eq.(5),

$$\frac{\varepsilon^{\mathrm{w_n}}_{\mathrm{Ex}}}{\varepsilon^{jf}_{\mathrm{DR}}} = \frac{C^{\mathrm{w_n}}_{\mathrm{Ex}}(T_e)}{F_1(T_e) F_2(j,f)} \qquad (9)$$

where the branching ratio for the heliumlike resonance line is assumed to be one, and recombination population of the upper levels of w_n has been ignored. For n=2, this ratio has been routinely used for electron temperature determination [15,24]. The advantage of using these line ratios is that the result is independent of the heliumlike charge state density.

The x-ray observations described in the following sections were obtained from the Alcator C-Mod [25] tokamak, a compact (minor radius a$\sim$22 cm, elongation $\kappa \leq$ 1.8), high field device with all molybdenum plasma facing components. All of the results here are for Ohmic deuterium plasmas, with the central plasma parameters in the range of $0.9\times10^{20}/\mathrm{m}^3 \leq \mathrm{n}_{e0} \leq 1.8\times10^{20}/\mathrm{m}^3$ and 900 eV $\leq \mathrm{T}_{e0} \leq$ 2600 eV.

The x-ray spectra presented were recorded by a five chord, independently spatially scannable, high resolution spectrometer array [26]. Each spectrometer has a resolving power, $\lambda/\Delta\lambda$, of 4000, a 2 cm spatial resolution and a luminosity function of 7 x 10^{-9} cm^2sr. Measured line widths are usually dominated by Doppler broadening. Recently, one of the five spectrometers has been fit with an ADP crystal, which has a 2d spacing of 10.640 Å, to allow access to longer wavelengths. In the present paper, high resolution x-ray observations in the wavelength range 2.98 Å$\leq \lambda \leq$ 4.52 Å are shown. Wavelength calibration [27] has been achieved after determining the instrumental dispersions in reference to H- and He-like argon, chlorine and sulphur lines and previously measured molybdenum [28] lines. Lines from hydrogenlike [29,30] ions are taken to have precise wavelengths, either measured or calculated. The accuracy of measured wavelengths described here is $\pm$0.3 mÅ, determined mainly from the quality of the line fits, and is less than the differences in various calculated Li-like wavelengths. The argon was puffed into the plasma through a piezo-electric valve and the chlorine was introduced by freon ($\mathrm{C_2Cl_3F_3}$) injection utilizing a fast scanning probe [31]. Chlorine is also present as an intrinsic impurity from solvents used to clean vacuum components. Presumably sulphur is a trace impurity in the molybdenum.

III. Chlorine Experimental Observations and Code Comparsions

To provide adequate chlorine levels in the plasma, freon (tri-chloro-tri-fluoro-ethane) has been injected using the fast scanning probe. Shown in Fig. 1 are the time histories of the electron and chlorine densities, the electron temperature and

the brightnesses of spectroscopic lines from fluorine (F^{6+}, 883.1 Å) and chlorine (Cl^{15+}, 4.44–4.50 Å) for a discharge that had freon injections at 0.5 and 0.8 seconds. The impurity confinement for these halogens is very similar to that for other non-recycling impurities injected by laser blow-off into L-mode plasmas [32]. At the beginning of the discharge there is substantial intrinsic chlorine and fluorine (from solvents and exposed teflon) present until the plasma becomes diverted around .25 s, when impurity penetration drastically decreases [33]. The chlorine density has been determined from the brightnesses of the n=2 to 1 transitions [14-16] of Cl^{15+} in a similar fashion to the argon density measurements [34]. The electron density was measured by a two color interferometer and the electron temperature was determined from electron cyclotron emission measurements.

An x-ray spectrum in the vicinity of the n=3 resonance line of Cl^{15+}, $1s^2\ {}^1S_0$ – $1s3p\ {}^1P_1$ (w_3), is shown in Fig. 2. The upper level is 0.75 $\left(1s_{1/2}3p_{3/2}\right)_1$ + 0.25 $\left(1s_{1/2}3p_{1/2}\right)_1$ in jj-coupling notation. This admixture of the two J=1 levels for 1snp has almost the exact same proportion (75:25) for all n values that have been checked ($n \leq 14$). Also visible in this spectrum is the intercombination line (y_3), $1s^2\ {}^1S_0$ – $1s3p\ {}^3P_1$, at 3794.7 mÅ, and four groups of unresolved satellites denoted A_3, B_3, A_3' and C_3. A_3 and A_3' have upper levels of the form 1s2p3p which are populated by dielectronic recombination of Cl^{15+}, while B_3 and C_3 have upper levels of the form 1s2s3p which can either be populated by dielectronic recombination or inner shell excitation of Cl^{14+}. The brightest chlorine lines contributing to the spectrum of Fig. 2 are listed in Table I, which includes the transition designations (jj-coupling), calculated wavelengths from MZ and RELAC, satellite capture energies (as in Eq.6), oscillator strengths/satellite intensity factors (Eq.7) and (inner shell) excitation rates (as in Eq.4, evaluated at 1500 eV).

Shown for comparison in the lower frame of Fig. 2 is a synthetic spectrum, generated with the calculated wavelengths from RELAC, Doppler (and instrumental) line widths and intensities from the collisional radiative model described above. The line intensities are determined from the emissivities of Eqs.4 and 5, using mea-

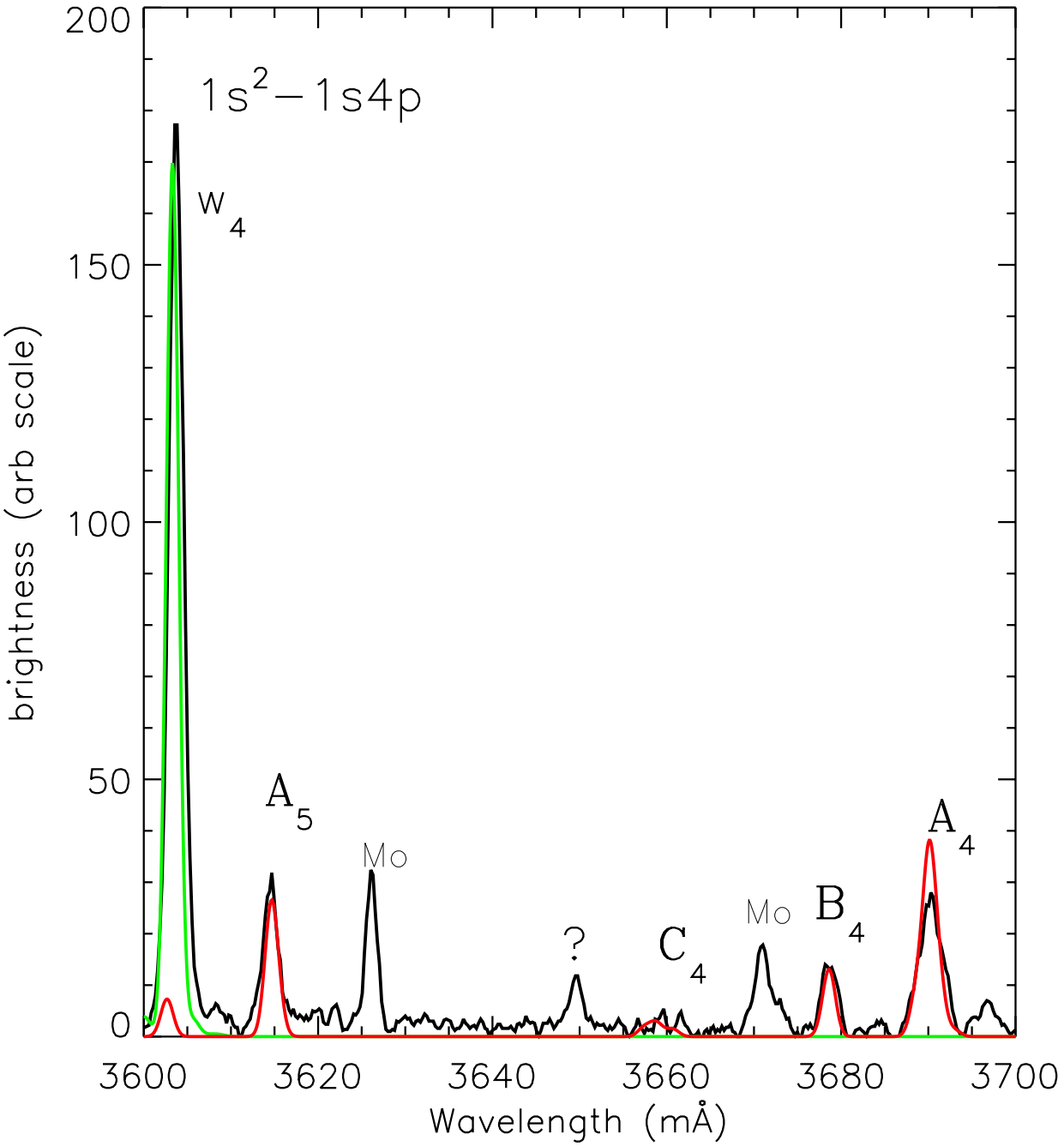
200
150
100
50
0
brightness (arb scale)
1s^2–1s4p
W$_4$
A$_5$
Mo
?
C$_4$
Mo
B$_4$
A$_4$
3600
3620
3640
3660
3680
3700
Wavelength (mÅ)

sured electron temperature and density profiles, with charge state density profiles calculated from the impurity transport code MIST [35] (including the appropriate impurity transport coefficients [32]). The line brightness is then determined by integrating the emissivity profile along the observation line of sight for each transition. The observed spectrum was obtained from a plasma which had a central electron temperature of 1200 eV and a central electron density of $1.8\times10^{20}/m^3$. The agreement between the calculated and the observed spectra is good. There is strong configuration interaction in the RELAC calculations between the 1s2p3p upper levels of the A_3 and A_3' transitions and the 1s2s3s and 1s2s3d levels. Here the configuration interaction "pushes up" or raises the 1s2p3p level energies. When the configuration interaction is turned off, the calculated wavelengths for the transitions making up A_3 and A_3' increase by about 3.5 mÅ (these shifted wavelengths are what is plotted in Fig. 2). This interaction is seen to diminish rapidly with increasing n. Molybdenum lines [28] at 3785.7, 3831.0 and 3834.6 mÅ contaminate this spectrum.

While the relative intensities calculated for the satellites are in good agreement, the predicted intensity for the intercombination line y_3 is too low. The observed ratio of y_3/w_3 is ~0.05 while the calculated value is ~0.030. This has also been observed in argon [7,6,8] and iron [36]. There is a predicted feature at 3810.5 mÅ that is due to lithiumlike transitions of the form $1s^23l - 1s3l3l'$. These satellites to the w_3 and y_3 lines are fed almost exclusively by dielectronic recombination from the ground level of Cl^{15+}, although some of the low-lying excited levels of that ion are also reachable by autoionization. Transitions of the type $1s^23l - 1s3lnl'$ for $n > 3$ appear on the long wavelength side of the w_3 line. Blending of these high-n satellites with the y_3 line may contribute to the underestimate of the y_3 intensity in the collisional-radiative model [7,8,36], however since the $1s^23l - 1s3l3l'$ feature is so weak, it is unlikely that this is the cause of the remaining discrepancy. There is a phenomenon that is known in the study of configuration interaction where the strength of a class of transitions is transfered to a higher energy class of transitions when the upper levels of the two classes are interacting [37]. This was seen with the

$2p^5_{1/2}6d$ and $2p^5_{3/2}7d$ levels in Ne-like Zr, Nb, Mo and Pd ions; when the $2p^5_{1/2}6d$ and $2p^5_{3/2}7d$ levels crossed, the direction of the strength transfer was reversed [38]. It could be that mixing between the two 1snp $^{1,3}P_1$ levels transfers strength from the (lower energy) $^3P_1$ level to the (higher energy) $^1P_1$ level, thus suppressing the y_3 line. There is no way to turn off this mixing in the RELAC calculations.

The corresponding spectrum near w_4 ($1s^2\ ^1S_0$ – $1s4p\ ^1P_1$) is shown in Fig.3, and two groups of satellites are apparent, A_4 and B_4, with a trace of C_4 (also A_5), in addition to molybdenum lines [28] at 3621.1 and 3671.0 mÅ. The line at 3649.6 mÅ is of unknown origin. A_4 is composed of lines which have upper levels of the form 1s2p4p which are populated by dielectronic recombination, while B_4 and C_4 have upper levels of the form 1s2s4p which can either be populated by dielectronic recombination or inner shell excitation. The transitions contributing to these satellite groups are summarized in Table II. This spectrum was obtained from a chord viewing 8 cm below the midplane (r/a=0.3) in a discharge that had $n_{e0} = 1.6\times10^{20}/m^3$ and $T_{e0} = 1260$ eV. Also shown in Fig.3 is a synthetic spectrum, as described above, with satellite wavelengths from MZ, and the agreement with the observed spectrum is very good. Moving to higher n, the spectrum near w_5 ($1s^2\ ^1S_0$ – $1s5p\ ^1P_1$) is shown in Fig.4, which also includes w_4 and the Cl^{16+} Ly_β doublet (the individual lines of which are unresolved). The satellite groups A_5 and C_5 are seen, but B_5 is hidden beneath w_4. As the w_n series crowds closer together in wavelength, so do the corresponding satellite groups, and A_6, B_6, A_7 and B_7 are also present in this spectrum. Tables III and IV include the relevant information for these lines. The synthetic spectrum using the satellite wavelengths from MZ is shown at the bottom for comparison, again with good agreement. T_{e0} and n_{e0} for the discharge for which this spectrum was obtained were 1260 eV and $1.6\times10^{20}/m^3$, respectively. Another mystery line, at 3570.4 mÅ, is present.

Finally, the Rydberg series with up to w_{14} resolved is shown in Fig. 5, for two different times during a 5.4 T, deuterium discharge. In the bottom frame is the spectrum from the early portion, when the discharge was limited, with n_{e0} =

$1.4\times10^{20}/m^3$ and T_{e0} = 1650 eV; there are molybdenum lines at 3439.2, 3442.8, 3445.0, 3447.8 and 3450.3 mÅ, respectively [28], which dominate over w_8. The spectrum in the top frame is from later in the discharge, with $n_{e0} = 1.6\times10^{20}/m^3$ and T_{e0} = 1260 eV, which also had argon injection, and satellites from w_3 in argon [7, and next section] cover the chlorine w_9, w_{10} and w_{14}. The dotted vertical lines show the calculated (RELAC) wavelengths. Between the two spectra, all the lines from w_7 to w_{14} are resolved. Two sets of calculated wavelengths, from RELAC and MZ, for the Rydberg series of Cl^{15+} are presented in Table V. The agreement between the two calculations is very good, with the largest differences of one part in 10^4, within the experimental uncertainty.

The measured wavelengths of the high n satellite groups (unresolved) in Cl^{14+} are also summarized in Table V, along with the wavelength differences between the observed satellite groups of a given n number and the corresponding resonance line calculated from RELAC. The theoretical wavelengths (RELAC) for the resonance lines for the Cl^{15+} Rydberg series have been used for the wavelength calibration. The measured wavelength differences between the resonance lines, w_n, and the satellite groups A_n, B_n and C_n, as a function of n are shown in Fig.6. The curves are the theoretical values, from the calculated wavelengths of Tables I–V; the solid lines represent the wavelengths from MZ while the dash-dot-dot-dot lines use the wavelengths from RELAC. These values are taken from the centroids of the calculated satellite groups, as shown in the synthetic spectra. Overall the agreement between theory and experiment is very good, although there is a systematic shift of about 3 mÅ for the A_n lines calculated from RELAC. This offset is possibly due to the configuration interaction in RELAC described above between the 1s2pnp and the 1s2sns and 1s2snd levels which raises the energy of the upper levels in the A_n transitions. The configuration interaction between 1s2s4p and 1s2p4s levels and between 1s2s5p and 1s2p5s levels causes the bumps in the C_n and B_n curves at n=4 and n=5, respectively.

IV. Argon Observations and Code Comparison

The corresponding high n transitions and satellites have also been observed in argon. Because argon is a recycling gas, it remains in the plasma for a much longer duration than the chlorine, which allows for weaker lines to be studied. Shown in Fig.7 is a spectrum from argon including w_4, w_5 and w_6 from Ar^{16+}, Ly_β from Ar^{17+} and the satellite groups A_5-A_{12}, B_5-B_8 and C_5-C_7. Plasma parameters for the discharge from which this spectrum was obtained were $n_{e0} = 1.3\times10^{20}/m^3$ and $T_{e0} = 1550$ eV. A synthetic spectrum using the calculated satellite wavelengths from MZ is shown in the bottom frame, and the agreement is quite good. The transition designations, calculated wavelengths, satellite capture energies, oscillator strengths/satellite intensity factors and inner shell excitation rates (evaluated at 2000 eV) for Ar^{15+} satellites between n=4 and n=12 may be found in Tables VI-X. The measured wavelength differences between the resonance lines, w_n, and the satellite groups A_n, B_n and C_n, as a function of n for argon are shown in Fig.8. Also shown are the theoretical values (curves), from the calculated wavelengths of Tables VI-X; the solid lines are from the MZ wavelengths and the dash-dot-dot-dot lines represent the wavelengths from RELAC. The agreement between the observed wavelengths and those calculated from MZ is excellent. This Figure may be compared to Fig.3 in Ref.[6]. The theoretical B_n and C_n RELAC curves are seen to undergo an appearent discontinuity at n = 8. The RELAC calculations for the energy of the 1s2snp levels that give rise to the B_n and C_n features show strong configuration interaction between the 1s2snp and the 1s2pns and 1s2pnd levels for $3 \leq n \leq 7$ that "pushes down" the energy of the 1s2snp levels. The calculations predict that this interaction is almost non-existent for $n \geq 8$, and thus, the upper levels of the B_n and C_n features "jump up" in energy. Again, the calculated wavelengths from RELAC for the A_n series are systematically shorter than the observations by about 2 mÅ. Here, the configuration interaction between the 1s2pnp and the 1s2snd and 1s2sns for $3 \leq n \leq 7$ "pushes up" the energy of the 1s2pnp levels. The measured wavelengths (and differences from the RELAC

resonance lines) of the observed satellite groups are presented in Table XI, along with two sets of calculated resonance line wavelengths. As in the chlorine case, the two calculations for the Rydberg series wavelengths for argon are in excellent agreement.

As demonstrated above, the calculated wavelengths for the heliumlike Rydberg series lines from MZ and RELAC are in excellent agreement. The agreement between the observed wavelengths and those calculated for the lithiumlike satellite groups B_n and C_n by the two methods is also quite good. For the satellite groups A_n, the observed wavelengths and the MZ calculations are also very good, while those from RELAC are systematically 2-3 mÅ too short. This may be due to residual Coulomb interactions among different terms of a single configuration in the upper levels of the A_n transitions. A comparison may also be made for the satellite intensity factors calculated via the two approaches. Shown in Fig.9 are the satellite intensity factors calculated from RELAC and MZ for the satellites of Ar^{15+}. There is excellent agreement for the transitions which contribute to A_n and B_n, over two orders of magnitude. In general, most of the points are within 20% of each other for the two calculations. The largest deviations are found for the transitions contributing to C_n, and in particular for C_3. However, for the plasma conditions considered here, where the population of the upper levels of C_3 is dominated by inner shell excitation of lithiumlike argon, it is difficult to distinguish between the F_2's computed by the two methods.

Spectra of w_4 and satellites for plasmas with different central electron temperatures are shown in Fig.10. As the temperature decreases, the intensities of the satellite groups (relative to w_4) increase; in the bottom frame with an electron temperature of less than 1000 eV, the satellite group A_4 is nearly as bright as the resonance line. Similar observations were made from Alcator C [5], from radial profile measurements; in fact near the plasma periphery, the satellite group A_5 was actually brighter than w_5. Also shown in the Figure are the corresponding synthetic spectra, generated as described above (using the MZ wavelengths), which have been

normalized to w_4. The relative intensities of the satellites A_4, B_4 and C_4 (and A_5) are well reproduced for these three different electron temperature plasmas, supporting the dielectronic recombination and inner shell excitation rates presented in the Tables. (A strong molybdenum [28] line at 3230.1 mÅ is visible in these spectra.)

There is evidence for the argon intercombination line y_4 on the long wavelength side of w_4. Shown in Fig.11 is the spectrum in the immediate vicinity of w_4; the observed spectrum is depicted by the asterisks. The solid green curve centered 3199.6 mÅ is the calculated resonance line, normalized at the peak, with the appropriate width from the instrumental resolution and Doppler broadening. The green curve centered at 3201.6 mÅ is the intercombination line y_4, with the calculated wavelength but with the observed intensity. Shown in purple are two heliumlike satellites to Ar^{17+} Ly_β, 1s2s $^1S_0$ – 2p3s $^1P_1$ and 1s2p $^1P_1$ – 2p3p $^1D_2$, with calculated wavelengths of 3197.7 and 3206.6 mÅ, respectively. [The former decay is enabled by configuration interaction between the 2p3s $^1P_1$ level and the 2s3p $^3P_1$ and 2s3p $^1P_1$ levels (the calculation of the interaction is actually carried out in intermediate coupling on jj-coupled basis functions). In the collisional-radiative model, at T_e = 2 keV these lines are excited more than 99% by dielectronic recombination from the ground level of the hydrogenlike ion.] The solid black curve is the composite calculated spectrum, which agrees well with the data points. Without inclusion of the theoretical y_4 line, there would be excess emission around 3202 mÅ. The actual best fit experimental wavelength for y_4 is 3201.3 mÅ, which agrees well with the calculation. The calculated ratio of y_4/w_4 for these discharge conditions (2050 eV and $1.1\times10^{20}/m^3$) is 0.029, whereas the observed ratio is around 0.05 in Fig.11. This may be related to the ratio y_3/w_3 observed to be a factor of two higher than predicted [7].

Spectra near the Ar^{16+} Rydberg series limit [5] are shown in Fig.12. The top spectrum was taken along the central chord of a plasma with $n_{e0} = 0.9\times10^{20}/m^3$ and T_{e0} = 2600 eV. The resonance lines from w_6 to w_{14} are clearly resolved, and there is a region of enhanced brightness from w_{15} up to the series limit at 3008.8 mÅ,

presumably due to unresolved lines. Along this chord, most of the line emission is from the plasma center where electron impact excitation is the dominant mechanism for populating the upper levels. The continuum at wavelengths shorter than the limit is greater than the continuum level between the resonance lines, and is due to radiative recombination [5]. Ar^{17+} Ly_γ near 2987.4 mÅ is also prominent. The corresponding spectrum from an identical plasma, but taken along a chord viewing through r/a = 0.67, where the electron temperature was 1100 eV and the electron density was $0.8\times10^{20}/m^3$, is shown in the middle frame of Fig.12. The lines are greatly reduced in intensity and the widths are very narrow due to the lower ion temperature. The intensities of w_9 and w_{10} are enhanced relative to the trend of decreasing intensity with increasing n number, which is due to population by charge exchange recombination with intrinsic neutral deuterium in the ground state, near the plasma edge [39,5]. Emission from the very high n levels (n > 25) is also visible just on the long wavelength side of series limit. Along this chord, however, the lines w_{11} through w_{14} are not visible. The viewing chord of the middle spectrum was 18.5 cm above the mid-plane in a discharge with a lower X-point. The spectrum shown in the bottom frame is from a somewhat similar plasma, from a chord viewing through r/a = 0.62, but 19.7 cm below the mid-plane, for a lower X-point discharge. In this case w_{10} is enhanced relative to the other w_n lines (due to population by charge exchange with intrinsic neutral deuterium in the ground state) and the feature on the long wavelength side of the limit is now dominant. This feature is from n numbers between 30 and 40, and is due to charge exchange between hydrogenlike argon and intrinsic neutral deuterium in the n=3 and n=4 excited states [39,5]. The reason that this feature is so prominent in the bottom of the plasma near the X-point is because the neutral density is concentrated there [24,33]. Why there is no feature from n∼20 at 3018 mÅ, which would be from charge exchange n=2 excited deuterium, is unknown. In this spectrum, w_{12} through w_{14} are again absent. Why w_{11} is visible here but not in the spectrum from above the midplane is not clear, but may be related to the fact that w_{10} is strong here, and w_9 was dominant in the middle spectrum. (The bottom spectrum was obtained from a different plasma on

a different day from a different spectrometer.)

V. Sulphur Observations and Code Comparison

Finally, the Rydberg series of heliumlike S^{14+} from w_5 to w_{13} is shown in Fig.13, which was obtained from a plasma with $n_{e0} = 2.0\times10^{20}/m^3$ and $T_{e0} = 1100$ eV. Unlike the cases of argon and chlorine, for sulphur the hydrogenlike Ly_β doublet is on the short wavelength side of w_5. Also apparent is a molybdenum line at 3834.8 mÅ [28], in addition to A_3 in Cl^{14+}. The wavelengths and oscillator strengths for the heliumlike lines calculated by RELAC and MZ are presented in Table XII, again with the wavelengths in excellent agreement. The simulated spectrum is also shown in Fig.13. The strongest components of the satellite groups A_n are the transitions of the form $1s^22p\ J=\frac{3}{2} - (1s2p_{3/2}np_{3/2})_{5/2}$ ($1s^22p\ ^2P_{\frac{3}{2}} - 1s2p(^3P)np\ ^2D_{\frac{5}{2}}$ in LS coupling notation). The wavelengths and satellite intensity factors for these transitions calculated from MZ and RELAC with $3 \leq n \leq 10$ for S^{13+} are presented in Table XIII. Similar to the cases for chlorine and argon, the RELAC wavelengths are ~ 3.5 mÅ longer, while the F_2 values are in excellent agreement. The sulphur levels in Alcator C-Mod are too low for these satellites to be measured.

VI. Conclusions

The high n Rydberg series of heliumlike Cl, Ar and S have been observed from Alcator C-Mod plasmas. The associated lithiumlike satellites up to n=12 for Cl and Ar have also been seen. Comparison of observed satellite wavelengths has been made with calculations from two different atomic structure codes, RELAC and MZ, and there is good agreement in general, although the A_ns from RELAC, with lower levels of the form $1s^22p$, differ by 2-3 mÅ. Calculated wavelengths for the heliumlike resonance lines, w_n, from the two different methods are in excellent agreement. The calculated intensities of the satellite groups relative to the resonance lines are also in good agreement with the observed line brightnesses, verifying the

dielectronic recombination and inner shell excitation rates. The large majority of the satellite intensity factors, F_2, computed by the two approaches, is within 20%. The intercombination line y_4 has been observed for argon.

VII. Acknowledgements

The authors would like to thank the Alcator C-Mod operations group for expert running of the tokamak. Work supported at MIT by DoE Contract No. DE-FC02-99ER54512 and at LLNL by DoE Contract No. W-7405-ENG-48.

References

[1] N.J.Peacock et al., J. Phys. B **2**, 798 (1969)

[2] P.G.Burkhalter et al., J. Appl. Phys. **50**, 4532 (1979)

[3] V.A.Boiko et al., J. Phys. B **10**, 3387 (1977)

[4] J.F.Seely and U.Feldman, Phys. Rev. Lett. **54**, 1016 (1985)

[5] J.E.Rice, E.S.Marmar, E.Källne and J.Källne, Phys. Rev. A **35**, 3033 (1987)

[6] E.Källne et al., Phys. Rev. A **38**, 2056 (1988)

[7] P.Beiersdorfer et al., Phys. Rev. E **52**, 1980 (1995)

[8] A.J.Smith et al., Phys. Rev. A **54**, 462 (1996)

[9] E.Källne et al., Phys. Rev. Lett. **49**, 330 (1982)

[10] L.A.Vainshtein and U.I.Safronova, At. Data Nucl. Data Tables **25**, 311 (1980)

[11] C.P.Bhalla and T.W.Tunnell, J. Quant. Spectrosc. Radiat. Transfer **32**, 141 (1984)

[12] M.H.Chen, At. Data Nucl. Data Tables **34**, 301 (1986)

[13] J.Nilsen, At. Data Nucl. Data Tables **38**, 339 (1988)

[14] J.E.Rice et al., Phys. Rev. A **22**, 310 (1980)

[15] E.Källne, J.Källne, E.S.Marmar and J.E.Rice, Phys. Scr. **31**, 551 (1985)

[16] I.H.Coffey et al., in *UV and X-ray Spectroscopy of Astrophysical and Laboratory Plasmas* Frontiers Science Series 15 (Universal Academy Press, Tokyo, 1996, Editors: K.Yamashita and T.Watanabe) p.431

[17] Bar-Shalom, A. and Klapisch, M., Computer Phys. Comm. **50**, 375 (1988)

[18] M.Klapisch, Comput. Phys. Commun. **2**, 239 (1971)

[19] M.Klapisch, J.L.Schwob, B.S.Fraenkel and J.Oreg, J. Opt. Soc. Am. **67**, 148 (1977)

[20] Oreg, J., Goldstein, W. H., Klapisch, M. and Bar-Shalom, A., Phys. Rev. A **44**, 1750 (1991)

[21] Bar-Shalom, A., Klapisch, M. and Oreg, J., Phys. Rev. A **38**, 1773 (1988)

[22] L.A.Vainshtein and U.I.Safronova, Physica Scripta **31**, 519 (1985)

[23] U.I.Safronova and J.Nilsen, J. Quant. Spectrosc. Radiat. Transfer **51**, 853 (1994)

[24] J.E.Rice et al., Rev. Sci. Instrum. **66**, 752 (1995)

[25] I.H.Hutchinson et al., Phys. Plasmas **1**, 1511 (1994)

[26] J.E.Rice and E.S.Marmar, Rev. Sci. Instrum. **61**, 2753 (1990)

[27] P.Beiersdorfer et al., Phys. Rev. A **34**, 1297 (1986)

[28] J.E.Rice et al., Phys Rev A **51**, 3551 (1995)

[29] G.W.Erickson, J. Phys. Chem. Ref. Data **6**, 831 (1977)

[30] E.S.Marmar et al., Phys. Rev. A **33**, 774 (1986)

[31] B.LaBombard et al., J. Nucl. Mater. **266-269**, 571 (1999)

[32] J.E.Rice et al., Phys. Plasmas **4**, 1605 (1997)

[33] J.E.Rice et al., Fusion Eng. Des. **34** and **35**, 159 (1997)

[34] J.E.Rice et al., Nucl. Fusion **37**, 241 (1997)

[35] R.A.Hulse, Nucl. Tech./Fus. **3**, 259 (1983)

[36] A.J.Smith et al., Phys. Rev. A **47**, 3073 (1993)

[37] P.Mandelbaum, M.Finkenthal, J.L.Schwob and M.Klapisch, Phys. Rev. A **35**, 5051 (1987)

[38] J.E.Rice et al., Phys Rev A **53**, 3953 (1996)

[39] J.E.Rice et al., Phys. Rev. Lett. **56**, 50 (1986)

Table Captions

Table I. The Cl^{15+} n=3 resonance and intercombination lines, with Cl^{14+} satellites. The transition designations (the largest basis function in the intermediate-coupling calculation), calculated wavelengths, satellite capture energies, oscillator strengths/satellite intensity factors and inner shell excitation rates (at 1500 eV) are given for the strongest lines. In the 3^{rd} and 4^{th} columns are the calculated wavelengths, in mÅ, from the MZ and RELAC codes, respectively. The satellite capture energies (from RELAC) in the 5^{th} column are in eV. For the resonance and intercombination lines, the entries in the 6^{th} column are the oscillator strengths (from RELAC), while for the satellites, the entries in the 6^{th} column are the satellite intensity factors, F_2, from Eq.(7) (RELAC), in units of s^{-1}. The units for the (inner shell) excitation rates (from RELAC) in the 7^{th} column are cm^3/s. Powers of 10 are in brackets,[ ].

Table II. The calculated Cl^{15+} n=4 resonance and intercombination lines, with Cl^{14+} satellites. The legend is similar to that in Table I.

Table III. The Cl^{15+} n=5 resonance and intercombination lines, with satellites.

Table IV. The Cl^{14+} satellites for n=6-10.

Table V. Two calculations of the Cl^{15+} Rydberg series wavelengths, from MZ in the 2^{nd} column and from RELAC in the 3^{rd} column. Measured satellite group wavelengths, and measured wavelength differences between the resonance lines and the satellite groups are in columns 4-9. All wavelengths are in mÅ.

Table VI. The Ar^{16+} n=4 resonance and intercombination lines, with satellites. The transition designations, wavelengths, satellite capture energies, oscillator strengths/satellite intensity factors and inner shell excitation rates (at 2000 eV) are given for the strongest lines. The legend is similar to that in Table I.

Table VII. The Ar^{16+} n=5 resonance and intercombination lines, with satellites.

Table VIII. The Ar^{16+} n=6 resonance and intercombination lines, with satellites.

Table IX. The Ar^{16+} n=7 resonance and intercombination lines, with satellites.

Table X. The Ar^{15+} satellites for n=8-12.

Table XI. Two calculations of the Ar^{16+} Rydberg series wavelengths, measured satellite group wavelengths, and measured wavelength differences between the resonance lines and the satellite groups. All wavelengths are in mÅ.

Table XII. Two calculations of the S^{14+} Rydberg series wavelengths (in mÅ), along with radiative transition probabilities (s^{-1}) and oscillator strengths.

Table XIII. Two calculations of the strongest components of the A_n series in S^{13+}, $1s^2 2p\ J=\frac{3}{2} - (1s2p_{3/2}np_{3/2})_{5/2}$. Wavelengths are given in columns 2 and 3, satellite intensity factors are presented in columns 4 and 5, capture energies from RELAC are shown in column 6 and in the last column are inner shell excitation rates (at 1500 eV) from RELAC.

Figure Captions

Fig. 1 The time histories of several parameters of interest for a discharge with freon injections at 0.5 and 0.8 seconds. In the top frame are the electron (solid green) and chlorine (dash-dot-dot-dot red, $\times 10^4$) densities, in the middle frame is the central electron temperature and in the lower frame are the lithiumlike (883 Å) fluorine (green) and heliumlike (4.44–4.50 Å) chlorine (red) line brightnesses, with an arbitrary scale.

Fig. 2 The observed x-ray spectrum of the heliumlike Cl^{15+} resonance line w_3 with the intercombination line y_3 and satellites is shown on a linear scale in the top frame. In the bottom frame is a log plot, including a simulated spectrum with w_3 and y_3 shown in green, and the satellite groups shown in red.

Fig. 3 The x-ray spectrum of the Cl^{15+} resonance line w_4 with satellites. The calculated He-like (Li-like) spectrum is shown in green (red).

Fig. 4 The x-ray spectrum of the Cl^{15+} resonance lines w_5 and w_4, with satellites, and hydrogenlike Cl^{16+} Ly_β. The simulated H-like, He-like and Li-like spectra are shown in purple, green and red, respectively.

Fig. 5 The high n series of Cl^{15+} with n between 7 and 14. The top spectrum includes some argon lines which obscure the transitions with n = 9, 10 and 14, while the bottom spectrum contains several molybdenum lines which dominate the n = 8 transition. The vertical dotted lines indicate the calculated wavelengths.

Fig. 6 The difference between the satellite group wavelengths and the resonance line wavelengths in Cl^{15+} as a function of n, for the three satellite groups. The measured values for A_n, B_n and C_n are depicted as red asterisks, green triangles and purple dots, respectively. The satellite group A'_3 is shown as the orange $\times$. The theoretical wavelength differences are shown by the appropriately colored curves,

with the calculated value for A'_3 (from RELAC) given by the orange dot. The solid lines are from MZ, while the dash-dot-dot-dot lines are from RELAC. The largest error bars are shown.

Fig. 7 The linear scale x-ray spectrum of heliumlike Ar^{16+} w_4, w_5 and w_6, with satellites, and hydrogenlike Ar^{17+} Ly_β, is shown in the top frame. In the bottom frame is the log scale observed spectrum (black) and the computed spectrum for Ar^{16+} (green), Ar^{17+} (purple) and Ar^{15+} (red).

Fig. 8 The difference between the satellite wavelengths and the resonance line wavelengths in Ar^{16+} as a function of n, for the three satellite groups, along with the theoretical wavelengths. The legend is the same as in Fig.6.

Fig. 9 The Ar^{15+} satellite intensity factors computed from RELAC (abscissa) and MZ (ordinate). The red asterisks, green triangles, orange $\times$s and purple dots are for the various transitions contributing to the satellite groups A_n, B_n, A'_n and C_n, respectively.

Fig. 10 The observed x-ray spectra of Ar^{16+} w_4 with satellites, for three different central electron temperatures, are shown in black. The calculated spectra for w_4, A_4 and A_5 are shown in red, C_4 in purple and B_4 in green.

Fig. 11 The observed spectrum in the immediate vicinity of w_4 in Ar^{16+} is shown by the asterisks. The solid green curves are the calculated lines for w_4 and y_4, the red curve is for the satellite group A_5 and the purple curves are for two satellites to Ly_β in Ar^{17+}. The solid black curve is the composite calculated spectrum.

Fig. 12 Spectra near the Ar^{16+} series limit. In the top frame is the spectrum from a central chord view, in the middle frame is a spectrum from an identical plasma with a view 18.5 cm above the midplane (r/a=.67) and in the bottom frame is a spectrum from a similar plasma with a view 19.7 cm below the midplane (r/a=.62).

The ionization limit is shown as the vertical line. The lower spectrum was cut off below 2990 mÅ.

Fig. 13 The Rydberg series of heliumlike S^{14+} for n≥5. In green (purple) is the simulated spectrum for S^{14+} (S^{15+}).

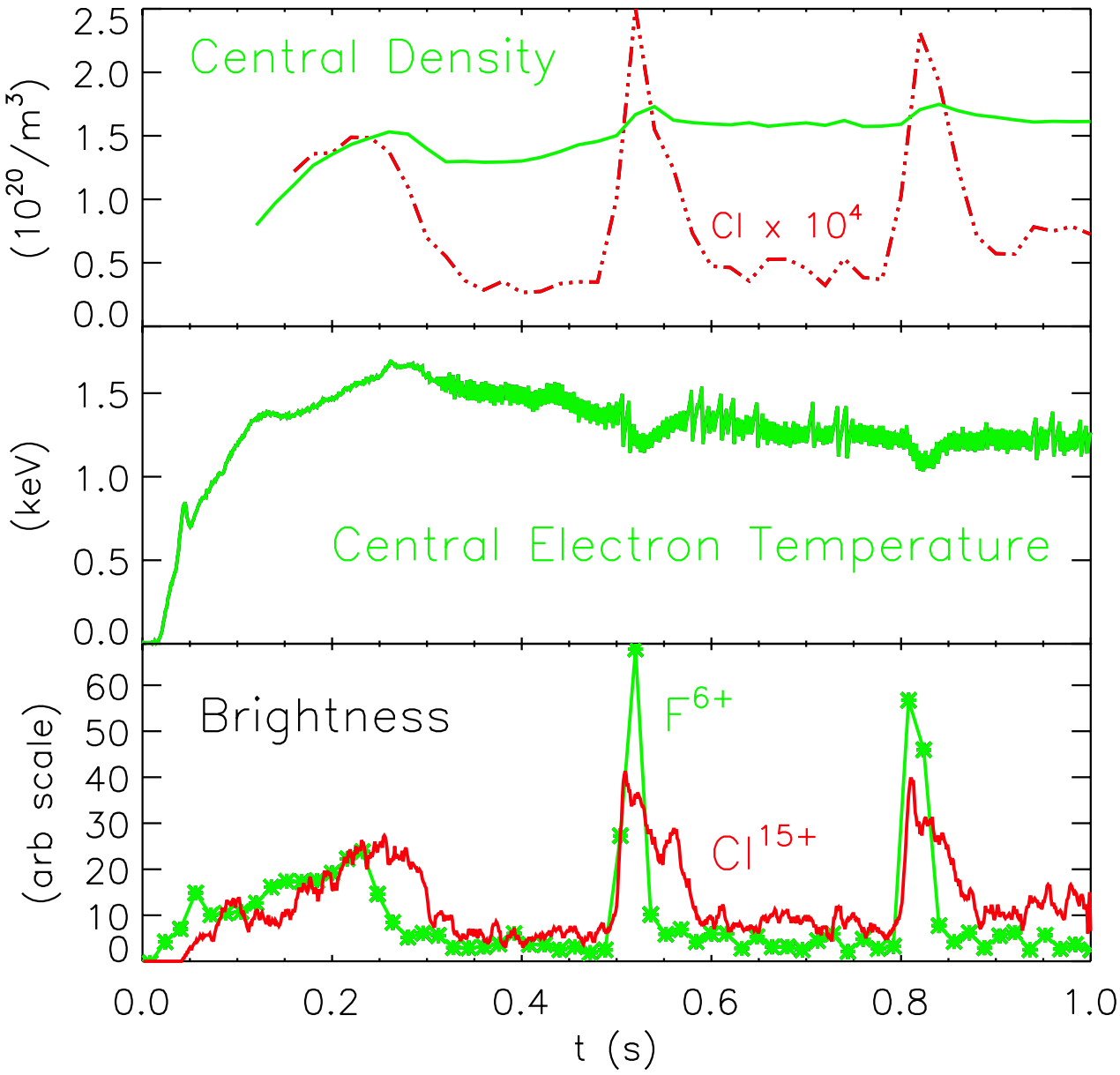
Central Density
Cl x 10^4
(10^20/m^3)
2.5
2.0
1.5
1.0
0.5
0.0
Central Electron Temperature
(keV)
1.5
1.0
0.5
0.0
Brightness
F^6+
Cl^15+
(arb scale)
60
50
40
30
20
10
0
0.0
0.2
0.4
0.6
0.8
1.0
t (s)

Figure 1

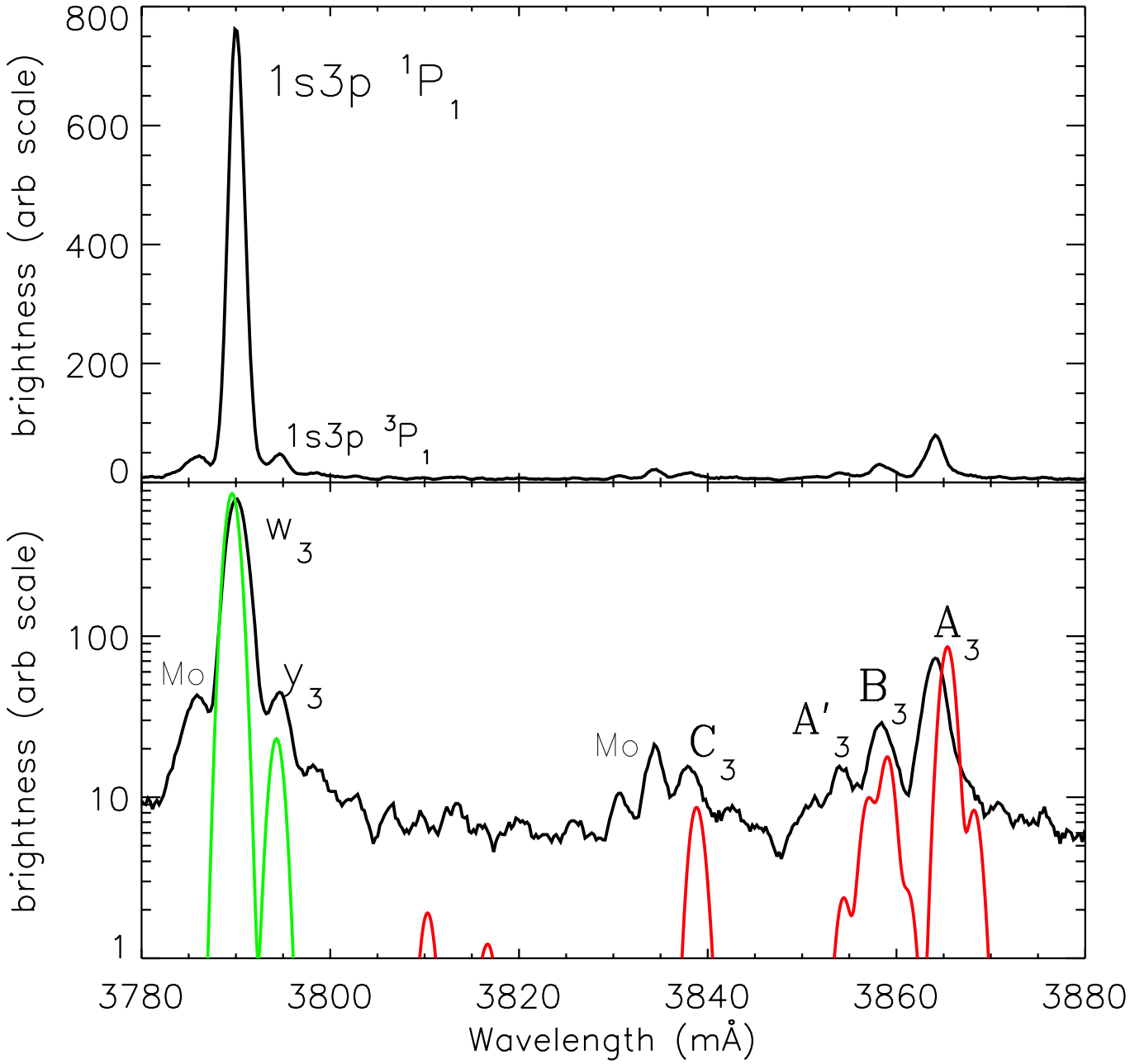
800
600
400
200
0
brightness (arb scale)
1s3p $^1P_1$
1s3p $^3P_1$
100
10
1
brightness (arb scale)
w_3
Mo
y_3
Mo
C_3
A'_3
B_3
A_3
3780
3800
3820
3840
3860
3880
Wavelength (mÅ)

Figure 2

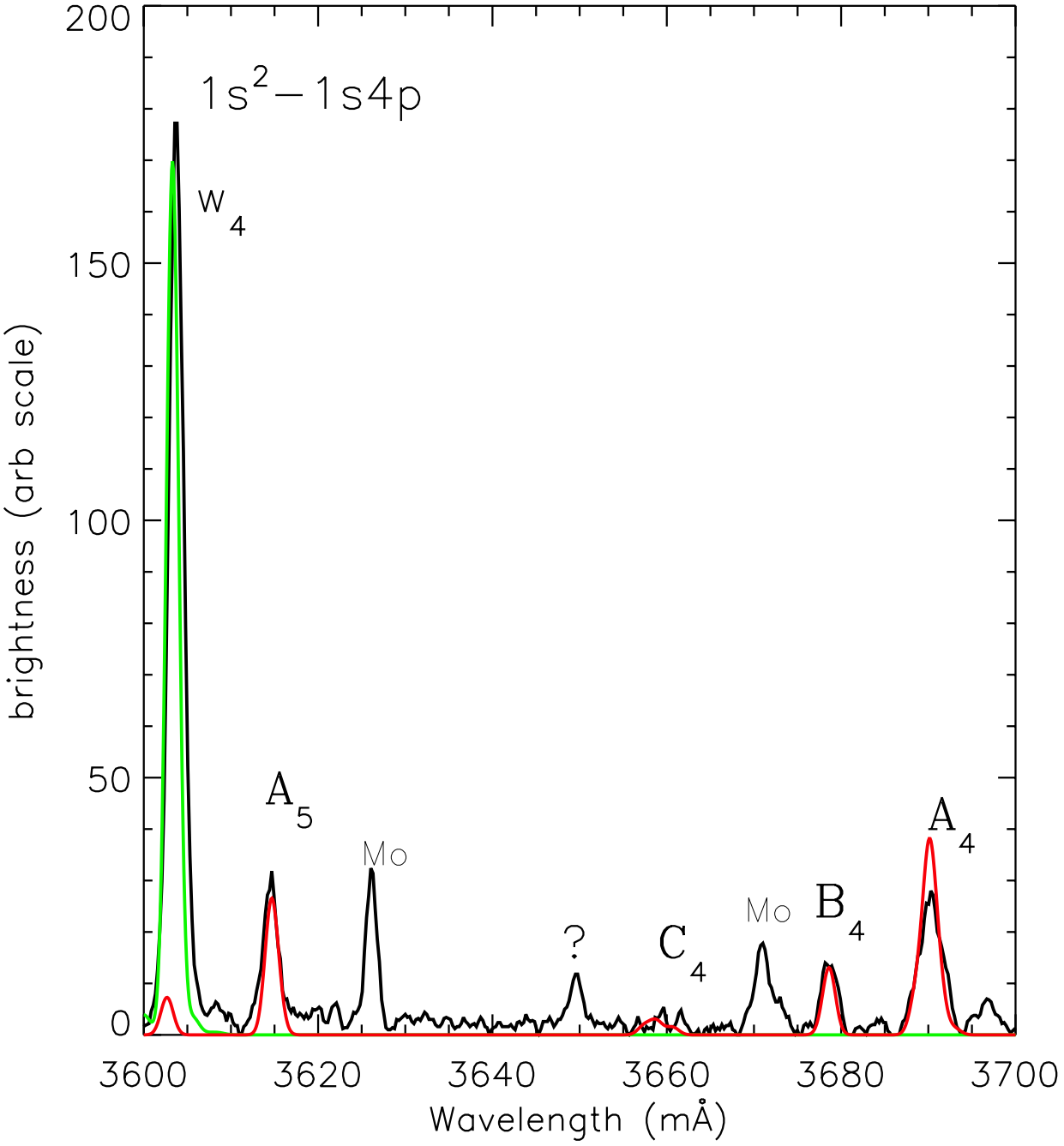
200
150
100
50
0
brightness (arb scale)
1s^2–1s4p
W$_4$
A$_5$
Mo
?
C$_4$
Mo
B$_4$
A$_4$
3600
3620
3640
3660
3680
3700
Wavelength (mÅ)

Figure 3

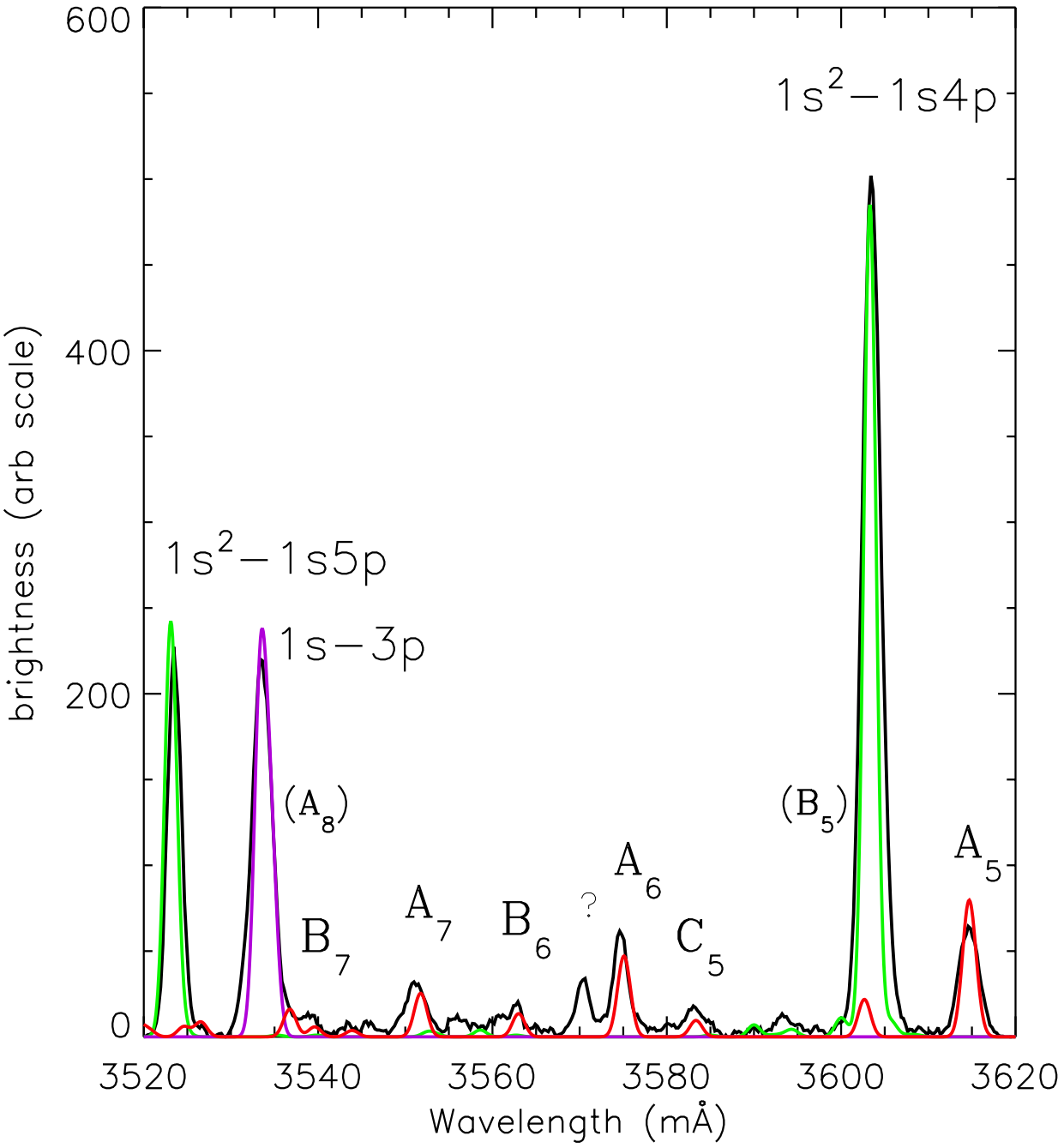
600
400
200
0
brightness (arb scale)
3520
3540
3560
3580
3600
3620
Wavelength (mÅ)
1s^2−1s4p
1s^2−1s5p
1s−3p
(A$_8$)
B$_7$
A$_7$
B$_6$
?
A$_6$
C$_5$
(B$_5$)
A$_5$

Figure 4

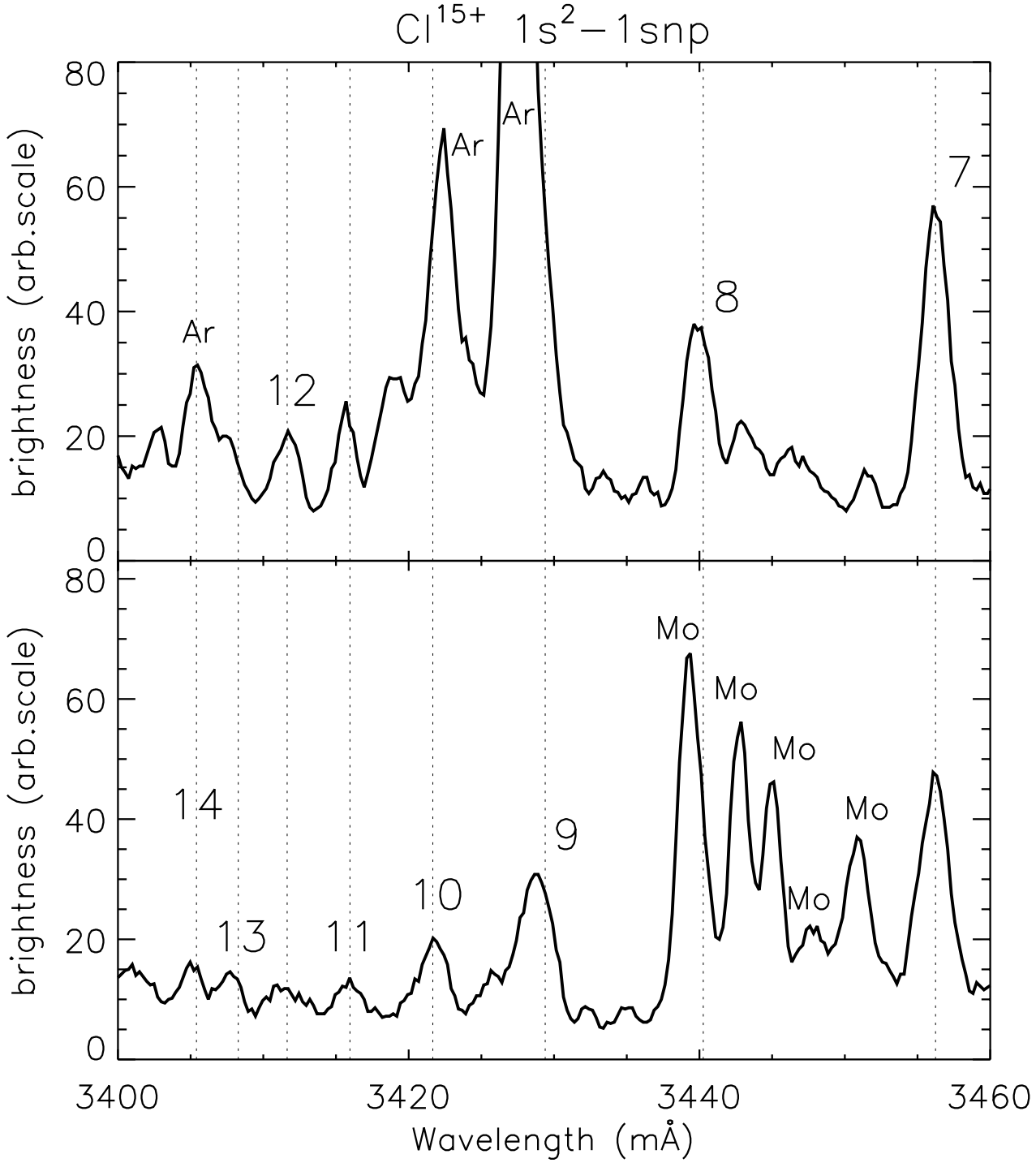
Cl15+ 1s2–1snp
brightness (arb.scale)
brightness (arb.scale)
Ar
Ar
Ar
12
8
7
14
13
11
10
9
Mo
Mo
Mo
Mo
Mo
0
20
40
60
80
3400
3420
3440
3460
Wavelength (mÅ)

Figure 5

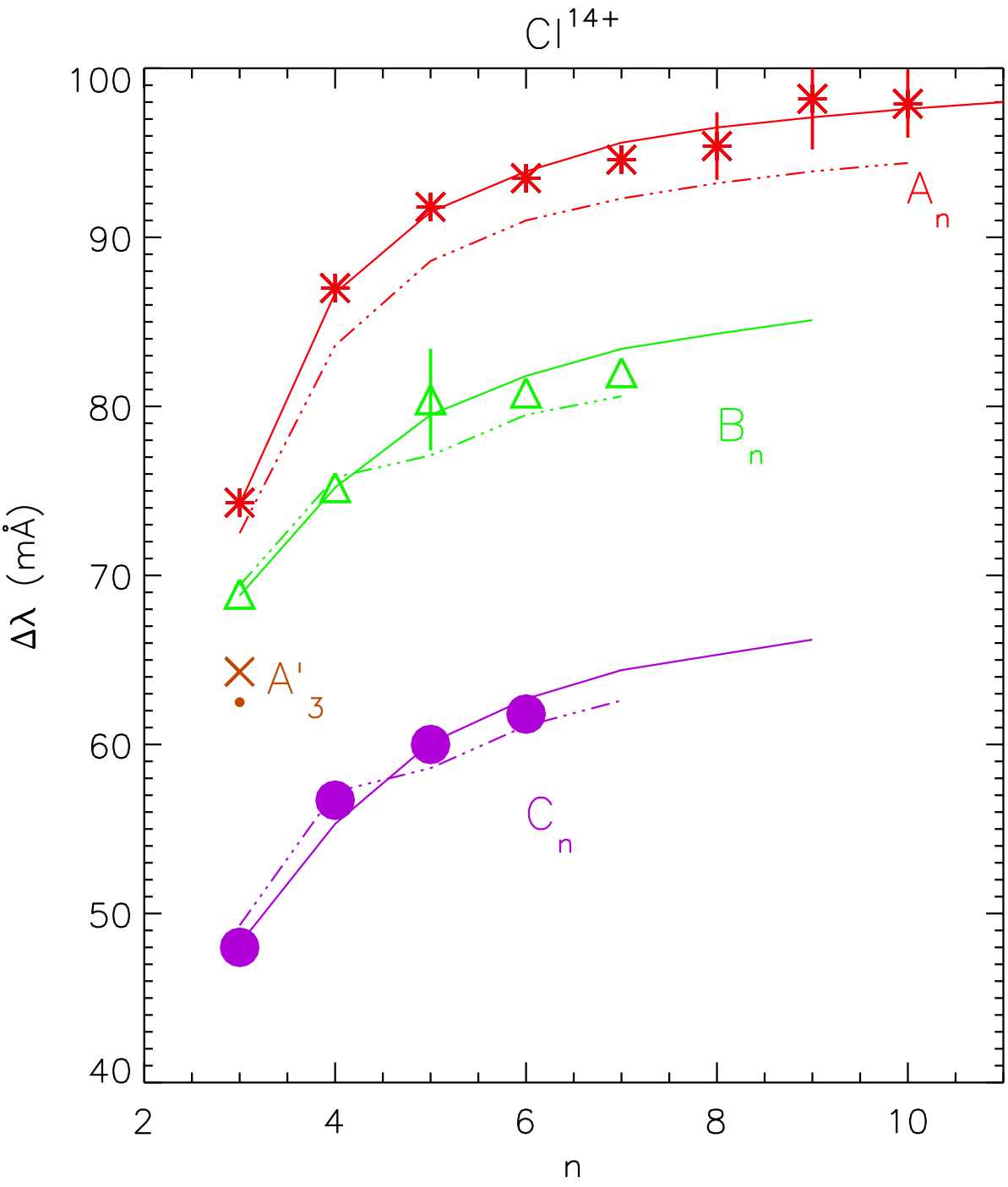

Figure 6

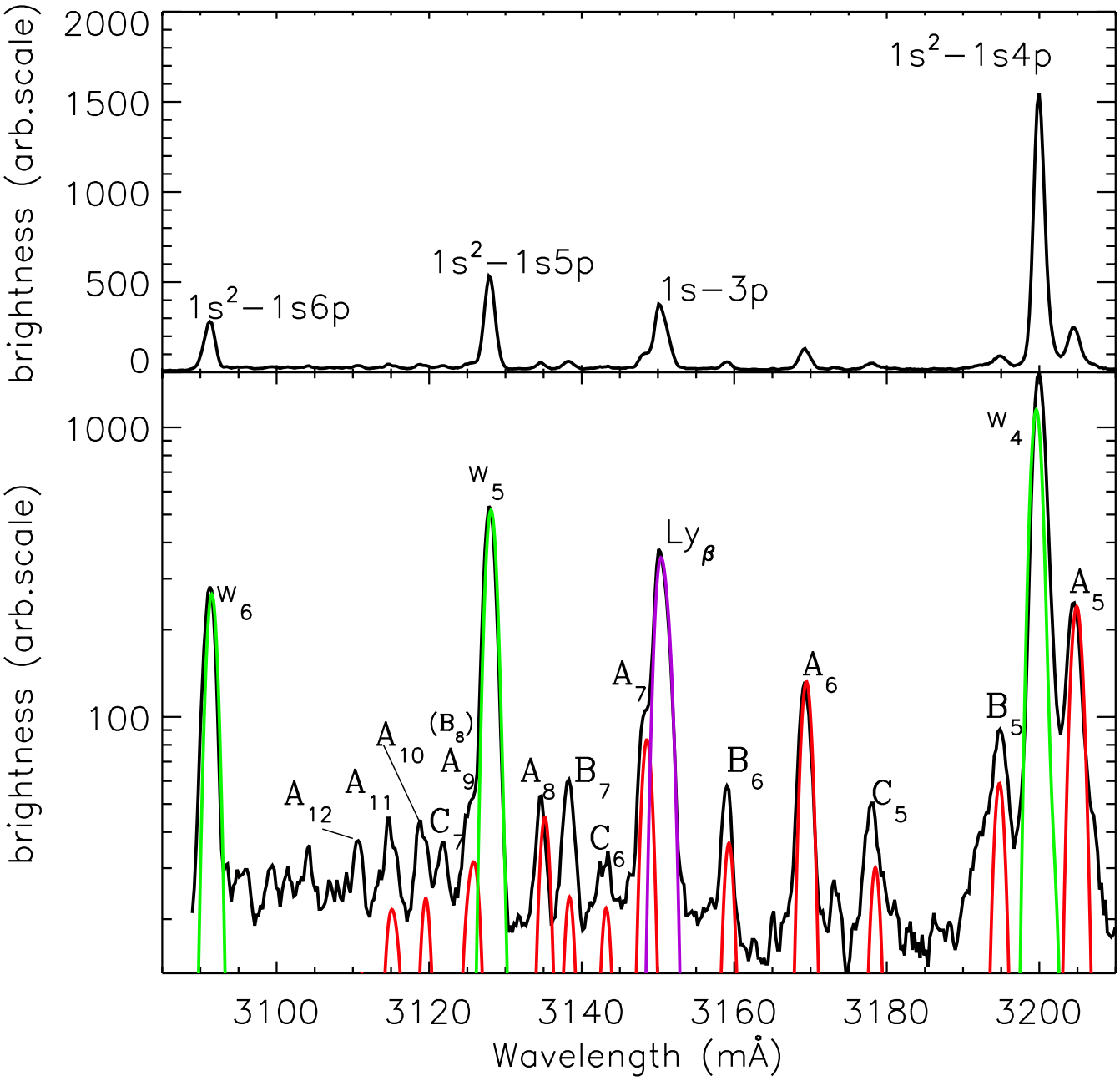
brightness (arb.scale)
2000
1500
1000
500
0
1s²−1s6p
1s²−1s5p
1s−3p
1s²−1s4p
brightness (arb.scale)
1000
100
w6
A12
A11
A10
(B8)
A9
C7
w5
A8
B7
C6
Lyβ
A7
B6
A6
C5
w4
B5
A5
3100
3120
3140
3160
3180
3200
Wavelength (mÅ)

Figure 7

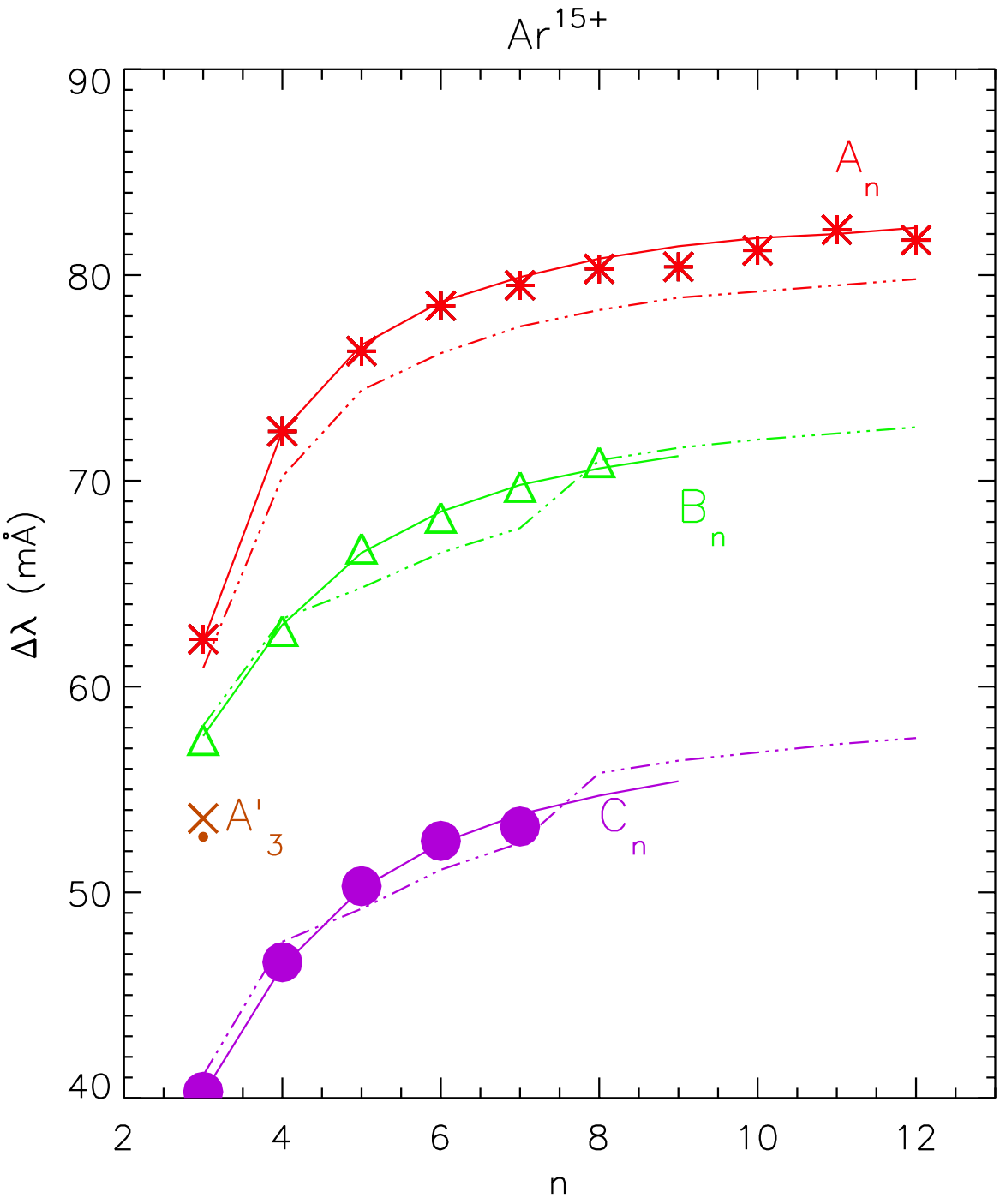

Figure 8

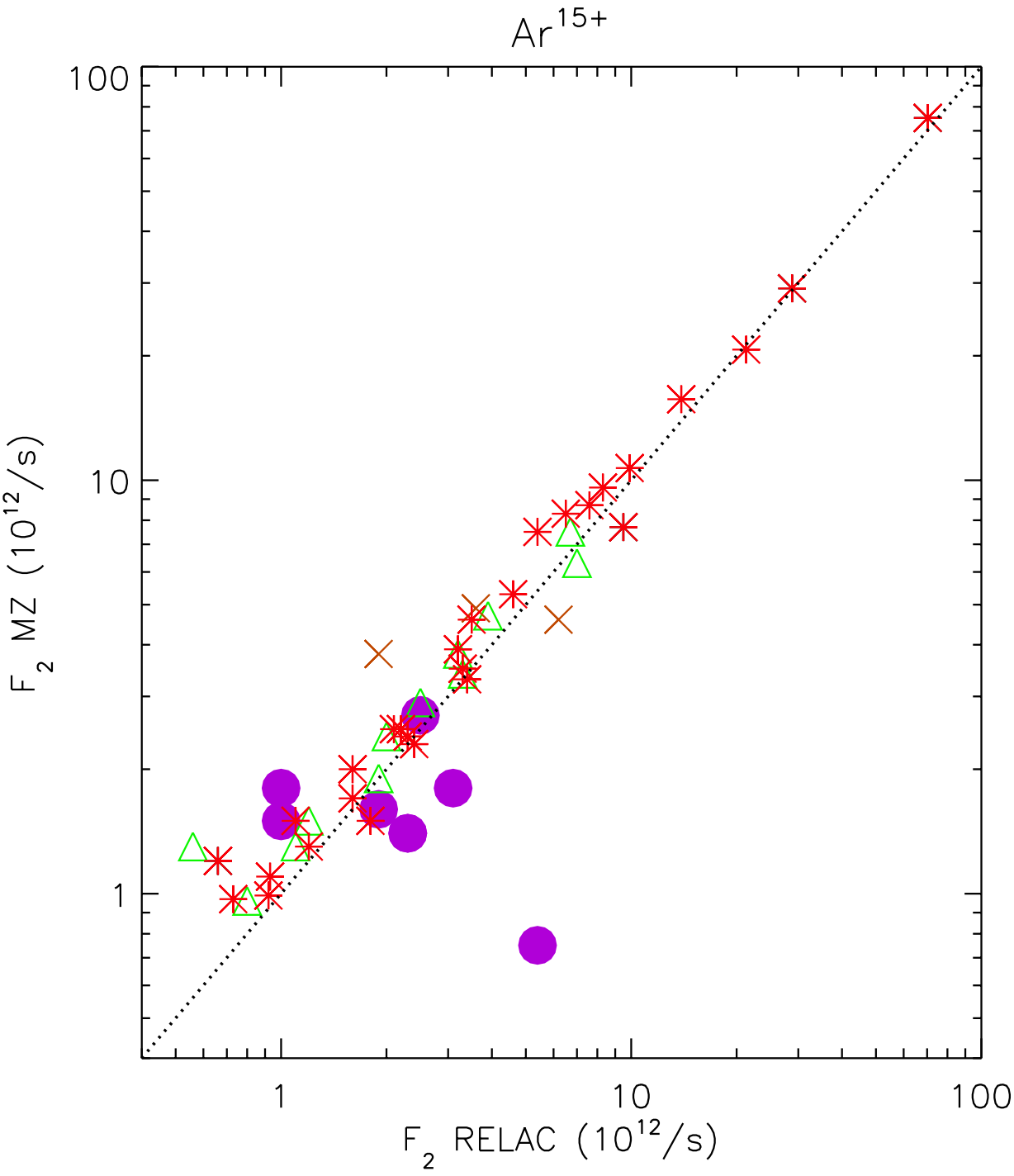

Figure 9

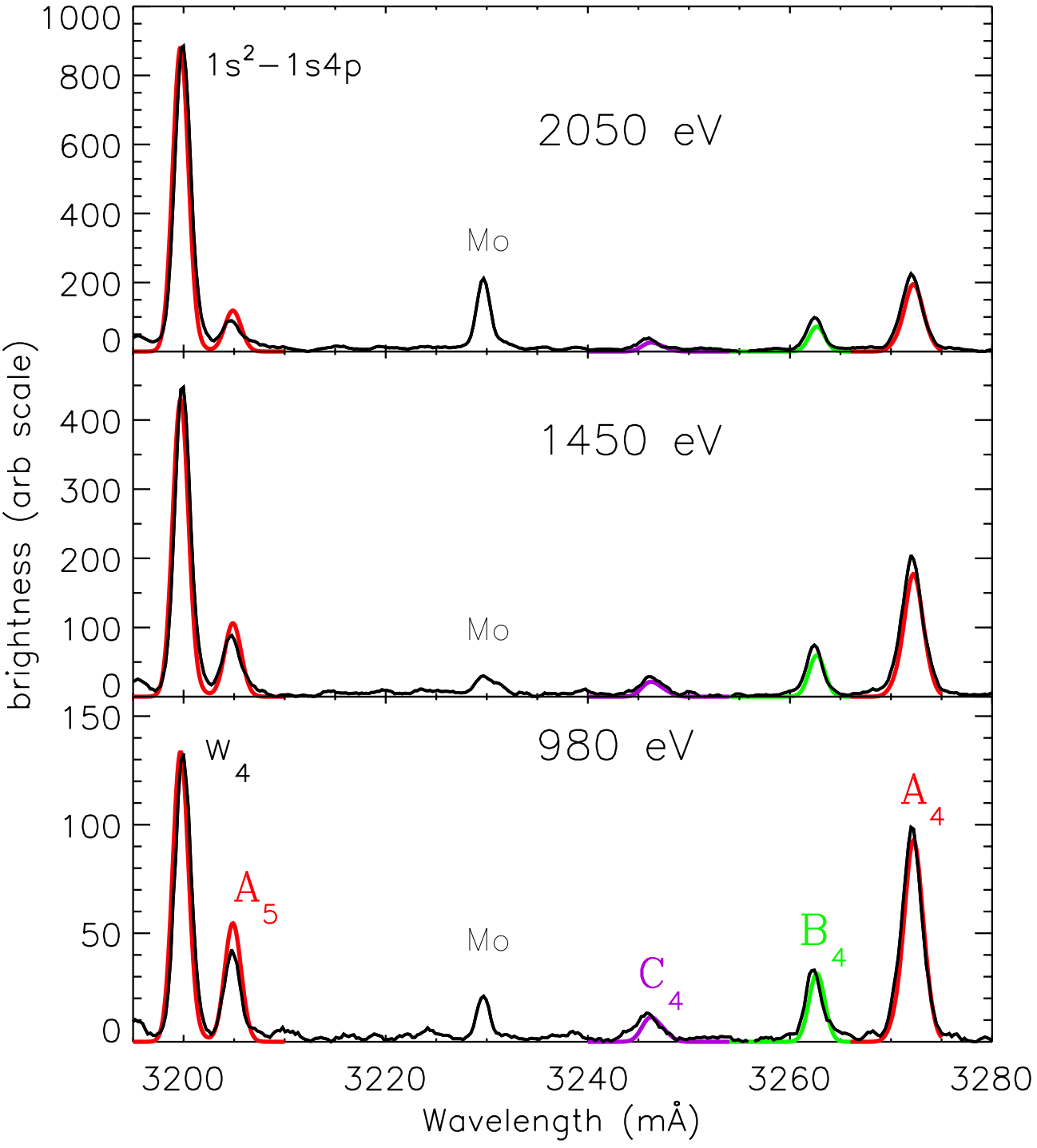
1000
800
600
400
200
0
1s²−1s4p
2050 eV
Mo
400
300
200
100
0
1450 eV
Mo
150
100
50
0
W4
980 eV
A5
A4
B4
C4
Mo
3200
3220
3240
3260
3280
Wavelength (mÅ)
brightness (arb scale)

Figure 10

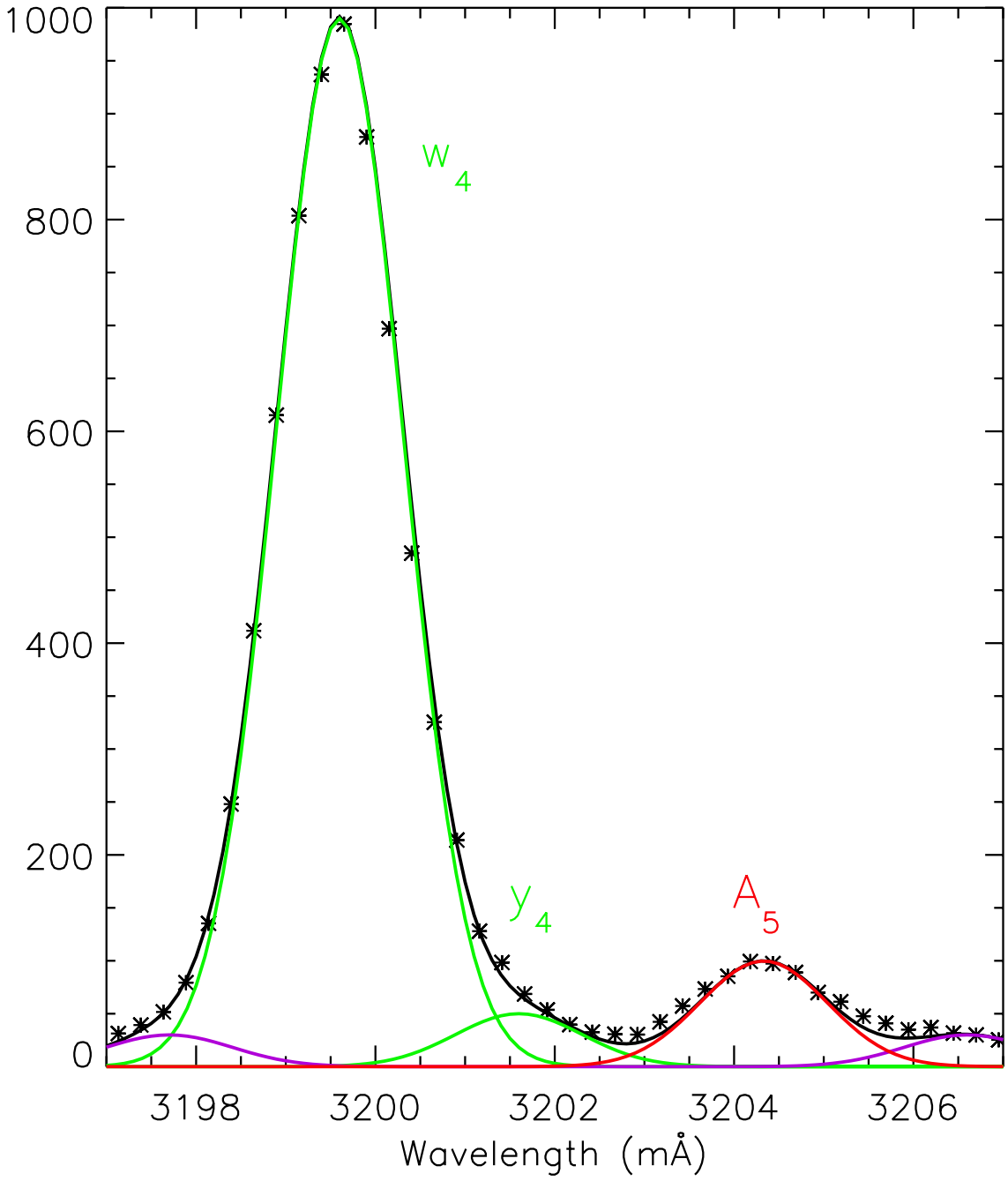
1000
800
600
400
200
0
W 4
y 4
A 5
3198
3200
3202
3204
3206
Wavelength (mÅ)

Figure 11

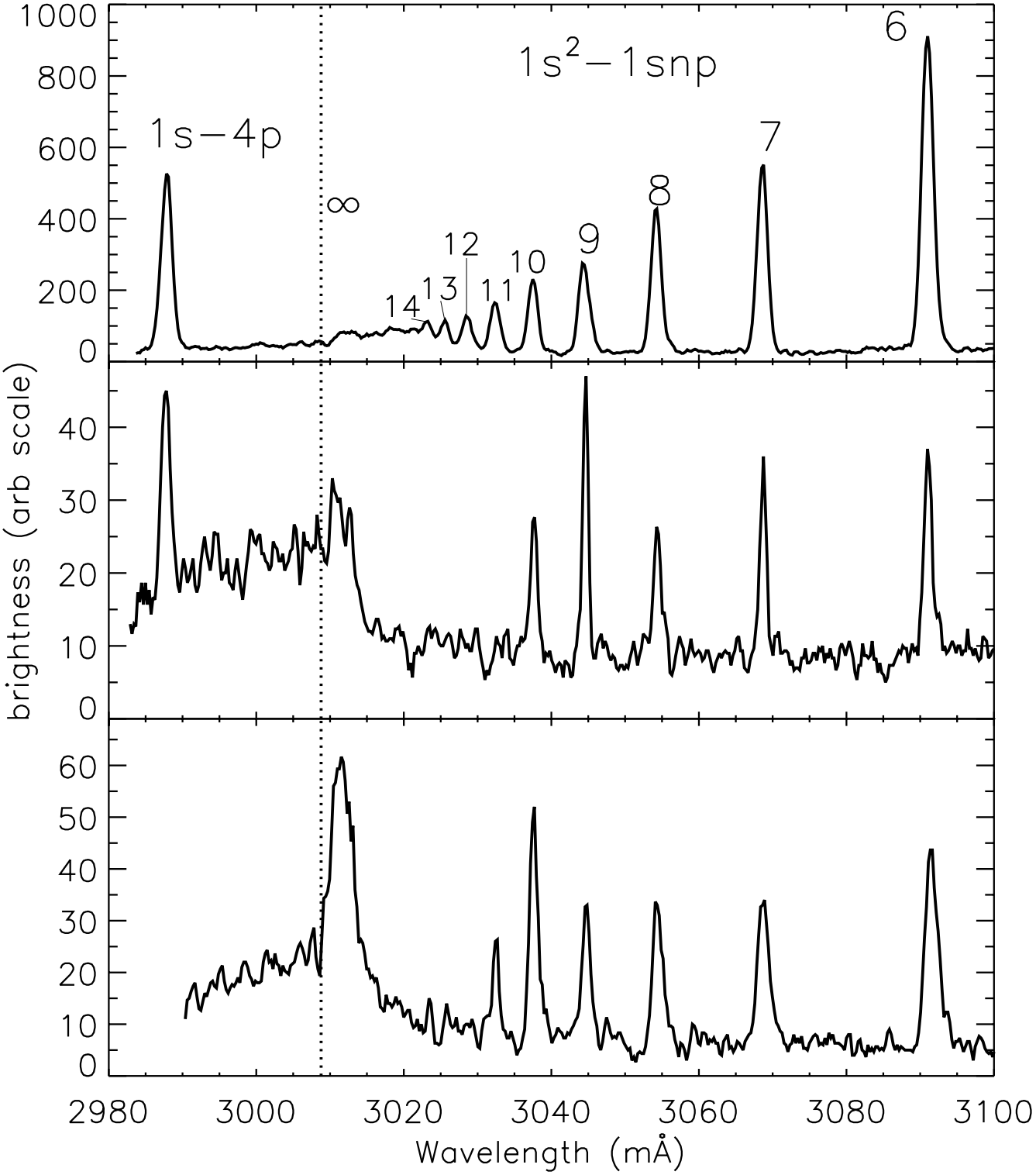
1000
800
600
400
200
0
1s−4p
1s²−1snp
∞
14
13
12
11
10
9
8
7
6
brightness (arb scale)
40
30
20
10
0
60
50
40
30
20
10
0
2980
3000
3020
3040
3060
3080
3100
Wavelength (mÅ)

Figure 12

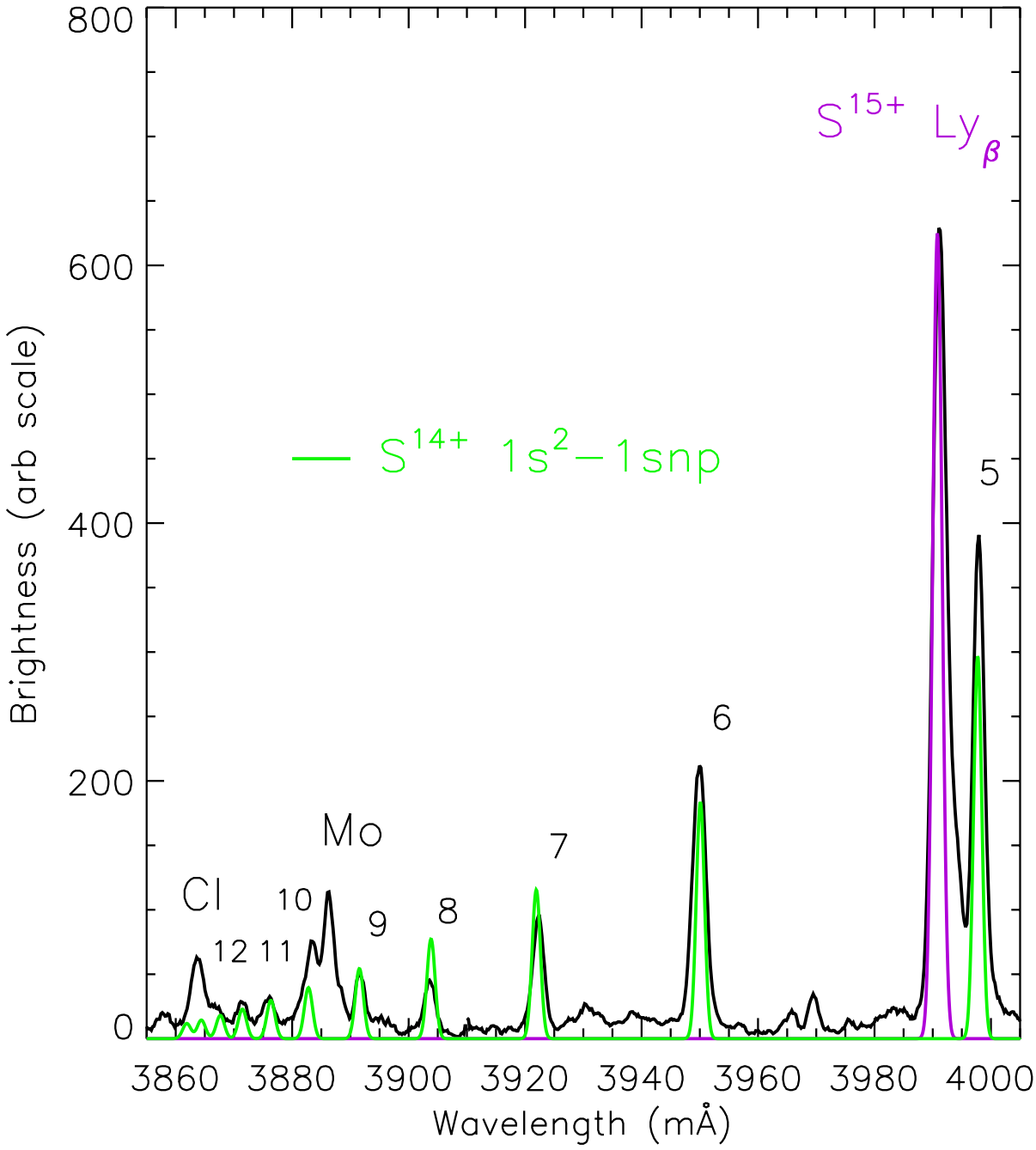
800
600
400
200
0
Brightness (arb scale)
3860
3880
3900
3920
3940
3960
3980
4000
Wavelength (mÅ)
S15+ Lyβ
S14+ 1s2–1snp
Cl
12
11
10
Mo
9
8
7
6
5

Figure 13

Table I. Cl^{15+} n=3 Lines with Satellites

Line	Transition	λ_{MZ} (mÅ)	λ_{Rel} (mÅ)		g*f	C_{Ex} (cm^3/s)
w_3	$1s^2\ ^1S_0$ - $1s3p\ ^1P_1$	3789.9	3789.6		1.635[−1]	4.275[−13]
y_3	$1s^2\ ^1S_0$ - $1s3p\ ^3P_1$		3794.3		1.490[−3]	6.459[−14]
				$\Delta E_{i,j}$(eV)	F_2(i,j) (s^{-1})	C_{IS} (cm^3/s)
C_3	$2s\ J=\frac{1}{2}$ - $(1s2s3p_{3/2})_{3/2}$	3838.1	3838.7	2420.89	4.90[+12]	1.178[−13]
C_3	$2s\ J=\frac{1}{2}$ - $(1s2s3p_{1/2})_{1/2}$	3838.9	3839.5	2420.15	2.35[+12]	6.445[−14]
A'_3	$2p\ J=\frac{3}{2}$ - $(1s2p_{3/2}3p_{3/2})_{3/2}$	3853.0	3854.2	2438.08	1.63[+12]	4.841[−14]
A'_3	$2p\ J=\frac{3}{2}$ - $(1s2p_{3/2}3p_{3/2})_{5/2}$	3853.9	3856.8	2440.23	5.70[+12]	4.169[−14]
A'_3	$2p\ J=\frac{3}{2}$ - $(1s2p_{3/2}3p_{1/2})_{3/2}$	3854.0	3857.1	2440.00	3.15[+12]	2.885[−14]
B_3	$2s\ J=\frac{1}{2}$ - $(1s2s3p_{3/2})_{1/2}$	3858.5	3859.0	2403.89	3.32[+12]	8.530[−14]
B_3	$2s\ J=\frac{1}{2}$ - $(1s2s3p_{3/2})_{3/2}$	3858.7	3859.1	2403.77	6.85[+12]	1.751[−13]
B_3	$2s\ J=\frac{1}{2}$ - $(1s2s3p_{1/2})_{3/2}$	3859.9	3861.2	2402.00	4.04[+11]	4.082[−14]
A_3	$2p\ J=\frac{1}{2}$ - $(1s2p_{1/2}3p_{3/2})_{3/2}$	3863.4	3865.2	2428.63	2.79[+13]	1.930[−13]
A_3	$2p\ J=\frac{3}{2}$ - $(1s2p_{3/2}3p_{3/2})_{5/2}$	3864.1	3865.5	2430.87	6.11[+13]	1.851[−13]
A_3	$2p\ J=\frac{3}{2}$ - $(1s2p_{1/2}3p_{3/2})_{3/2}$	3866.4	3868.2	2428.63	8.18[+12]	2.866[−14]

Table II. Cl^{15+} n=4 Lines with Satellites

Line	Transition	λ_{MZ} (mÅ)	λ_{Rel} (mÅ)		g*f	C_{Ex} (cm^3/s)
w_4	$1s^2\ {}^1S_0$ - $1s4p\ {}^1P_1$	3603.5	3603.3		6.436[−2]	1.422[−13]
y_4	$1s^2\ {}^1S_0$ - $1s4p\ {}^3P_1$	3605.3	3605.7		5.913[−4]	2.306[−14]
				$\Delta E_{i,j}$(eV)	F_2(i,j) (s^{-1})	C_{IS} (cm^3/s)
C_4	2s J=$\frac{1}{2}$ - $(1s2s4p_{3/2})_{3/2}$	3659.5	3660.5	2578.12	3.10[+12]	2.590[−14]
A'_4	2p J=$\frac{3}{2}$ - $(1s2p_{3/2}4p_{3/2})_{5/2}$	3678.1	3675.6	2596.53	1.36[+12]	2.102[−14]
A'_4	2p J=$\frac{3}{2}$ - $(1s2p_{3/2}4p_{1/2})_{3/2}$		3675.8	2596.38	4.79[+12]	9.147[−15]
B_4	2s J=$\frac{1}{2}$ - $(1s2s4p_{3/2})_{1/2}$	3678.6	3679.1	2560.99	3.06[+12]	3.144[−14]
B_4	2s J=$\frac{1}{2}$ - $(1s2s4p_{3/2})_{3/2}$	3678.7	3679.2	2560.90	6.26[+12]	6.160[−14]
A_4	2p J=$\frac{3}{2}$ - $(1s2p_{3/2}4p_{3/2})_{1/2}$	3688.5	3685.7	2587.30	3.22[+12]	1.422[−14]
A_4	2p J=$\frac{1}{2}$ - $(1s2p_{3/2}4p_{3/2})_{3/2}$	3688.6	3685.8	2584.83	3.69[+12]	1.780[−14]
A_4	2p J=$\frac{3}{2}$ - $(1s2p_{1/2}4f_{5/2})_{5/2}$	3689.6	3686.7	2586.49	6.05[+12]	1.264[−14]
A_4	2p J=$\frac{3}{2}$ - $(1s2p_{3/2}4p_{3/2})_{5/2}$	3690.2	3687.0	2586.15	1.78[+13]	3.336[−14]
A_4	2p J=$\frac{1}{2}$ - $(1s2p_{1/2}4p_{3/2})_{3/2}$	3690.3	3687.4	2583.30	6.58[+12]	4.109[−14]
A_4	2p J=$\frac{3}{2}$ - $(1s2p_{3/2}4p_{3/2})_{3/2}$	3691.3	3688.4	2584.83	7.94[+12]	2.096[−14]

Table III. Cl^{15+} n=5 Lines with Satellites

Line	Transition	λ_{MZ} (mÅ)	λ_{Rel} (mÅ)		g*f	C_{Ex} (cm^3/s)
w_5	$1s^2\ {}^1S_0$ - $1s5p\ {}^1P_1$	3523.2	3523.1		3.359[−2]	6.742[−14]
y_5	$1s^2\ {}^1S_0$ - $1s5p\ {}^3P_1$	3524.1	3524.6		3.042[−4]	1.070[−14]
				$\Delta E_{i,j}$(eV)	F_2(i,j) (s^{-1})	C_{IS} (cm^3/s)
C_5	2s J=$\frac{1}{2}$ - $(1s2s5p_{3/2})_{3/2}$	3583.4	3581.7	2652.56	2.54[+12]	1.362[−14]
B_5	2s J=$\frac{1}{2}$ - $(1s2s5p_{3/2})_{1/2}$	3602.6	3600.3	2634.77	1.80[+12]	1.533[−14]
B_5	2s J=$\frac{1}{2}$ - $(1s2s5p_{3/2})_{3/2}$	3602.7	3600.3	2634.73	3.65[+12]	2.999[−14]
A_5	2p J=$\frac{3}{2}$ - $(1s2p_{3/2}5p_{3/2})_{1/2}$	3614.2	3611.1	2656.79	2.19[+12]	7.045[−15]
A_5	2p J=$\frac{1}{2}$ - $(1s2p_{1/2}5p_{3/2})_{3/2}$	3614.5	3611.7	2653.85	3.82[+12]	1.939[−14]
A_5	2p J=$\frac{3}{2}$ - $(1s2p_{3/2}5p_{3/2})_{5/2}$	3614.7	3611.7	2656.27	1.17[+13]	2.122[−14]
A_5	2p J=$\frac{3}{2}$ - $(1s2p_{3/2}5p_{3/2})_{3/2}$	3615.4	3612.4	2655.59	3.56[+12]	1.152[−14]

Table IV. Cl^{14+} n=6, 7, 8, 9 and 10 Satellites

Line	Transition	λ_{MZ} (mÅ)	λ_{Rel} (mÅ)	$\Delta E_{i,j}$(eV)	F_2(i,j) (s^{-1})	C_{IS} (cm^3/s)
C_6	2s J=$\frac{1}{2}$ - $(1s2s6p_{3/2})_{3/2}$	3543.9	3542.3	2691.06	1.57[+12]	6.819[−15]
B_6	2s J=$\frac{1}{2}$ - $(1s2s6p_{3/2})_{3/2}$	3563.0	3560.7	2673.01	2.23[+12]	1.595[−14]
A_6	2p J=$\frac{1}{2}$ - $(1s2p_{1/2}6p_{3/2})_{3/2}$	3574.9	3572.1	2691.86	3.10[+12]	1.356[−14]
A_6	2p J=$\frac{3}{2}$ - $(1s2p_{3/2}6p_{3/2})_{5/2}$	3575.1	3572.2	2694.17	6.41[+12]	1.106[−14]
A_6	2p J=$\frac{3}{2}$ - $(1s2p_{3/2}6p_{3/2})_{3/2}$	3575.5	3572.6	2693.80	2.11[+12]	6.842[−15]
B_7	2s J=$\frac{1}{2}$ - $(1s2s7p_{3/2})_{3/2}$	3539.6	3537.3	2696.08	1.75[+12]	9.507[−15]
A_7	2p J=$\frac{3}{2}$ - $(1s2p_{3/2}7p_{3/2})_{5/2}$	3551.8	3548.9	2717.03	3.88[+12]	6.638[−15]
A_8	2p J=$\frac{3}{2}$ - $(1s2p_{3/2}8p_{3/2})_{5/2}$	3536.8	3533.9	2731.67	2.79[+12]	4.399[−15]
A_9	2p J=$\frac{3}{2}$ - $(1s2p_{3/2}9p_{3/2})_{5/2}$	3526.5	3523.7	2741.85	1.93[+12]	3.015[−15]
A_{10}	2p J=$\frac{3}{2}$ - $(1s2p_{3/2}10p_{3/2})_{5/2}$	3519.3	3516.5	2749.13	1.39[+12]	2.169[−15]

Table V. Calculated Cl^{15+} Rydberg Series and Measured Cl^{14+} High n Satellites

n	W_n		C_n		B_n		A_n [A'_3]	
	λ_{MZ}	λ_{Rel}	λ_{Exp}	$\Delta\lambda$	λ_{Exp}	$\Delta\lambda$	λ_{Exp}	$\Delta\lambda$
3	3789.9	3789.6	3837.6	48.0	3858.5	68.9	3863.9	74.3
							[3853.9]	[64.3]
4	3603.5	3603.3	3660.0	56.7	3678.5	75.2	3690.3	87.0
5	3523.2	3523.1	3583.1	60.0	(3603.5)	(80.4)	3614.9	91.8
6	3481.2	3481.2	3543.0	61.8	3562.0	80.8	3574.7	93.5
7	3456.2	3456.6			3538.6	82.0	3551.2	94.6
8	3440.3	3440.7					(3536.)	(95)
9	3429.4	3429.8					3528.0	98.2
10	3421.7	3422.1					3520.0	97.9
11	3416.0	3416.4						
12	3411.6	3412.1						
13	3408.3	3408.7						
14	3405.4	3406.1						

Table VI. Ar^{16+} n=4 Lines with Satellites

Line	Transition	λ_{MZ} (mÅ)	λ_{Rel} (mÅ)		g*f	C_{Ex} (cm^3/s)
w_4	$1s^2\ {}^1S_0$ - $1s4p\ {}^1P_1$	3199.7	3199.6		6.364[−2]	1.659[−13]
y_4	$1s^2\ {}^1S_0$ - $1s4p\ {}^3P_1$	3201.2	3201.6		8.162[−4]	2.466[−14]
				$\Delta E_{i,j}$(eV)	F_2(i,j) (s^{-1})	C_{IS} (cm^3/s)
C_4	$2s\ J=\frac{1}{2}$ - $(1s2p_{1/2}4s)_{3/2}$	3245.9	3246.6	2900.69	2.49[+12]	1.067[−14]
C_4	$2s\ J=\frac{1}{2}$ - $(1s2s4p_{3/2})_{3/2}$	3246.4	3247.4	2899.80	2.32[+12]	2.384[−14]
C_4	$2s\ J=\frac{1}{2}$ - $(1s2s4p_{1/2})_{1/2}$	3247.5	3247.4	2899.77	2.32[+12]	1.219[−14]
B_4	$2s\ J=\frac{1}{2}$ - $(1s2s4p_{3/2})_{1/2}$	3262.6	3262.9	2881.61	3.21[+12]	3.521[−14]
B_4	$2s\ J=\frac{1}{2}$ - $(1s2s4p_{3/2})_{3/2}$	3262.7	3263.0	2881.50	6.71[+12]	6.979[−14]
A_4	$2p\ J=\frac{1}{2}$ - $(1s2p_{3/2}4p_{3/2})_{3/2}$	3270.6	3268.4	2907.36	2.21[+12]	1.167[−14]
A_4	$2p\ J=\frac{3}{2}$ - $(1s2p_{3/2}4p_{3/2})_{1/2}$	3271.0	3268.8	2910.37	3.39[+12]	1.613[−14]
A_4	$2p\ J=\frac{3}{2}$ - $(1s2p_{3/2}4p_{3/2})_{5/2}$	3272.0	3269.9	2909.02	2.13[+13]	3.902[−14]
A_4	$2p\ J=\frac{1}{2}$ - $(1s2p_{1/2}4p_{3/2})_{3/2}$	3272.3	3270.1	2905.45	9.86[+12]	5.520[−14]
A_4	$2p\ J=\frac{3}{2}$ - $(1s2p_{1/2}4f_{5/2})_{5/2}$	3272.4	3270.1	2908.51	6.45[+12]	1.426[−14]
A_4	$2p\ J=\frac{3}{2}$ - $(1s2p_{3/2}4p_{3/2})_{3/2}$	3273.3	3271.1	2907.36	8.25[+12]	2.413[−14]

Table VII. Ar^{16+} n=5 Lines with Satellites

Line	Transition	λ_{MZ} (mÅ)	λ_{Rel} (mÅ)		g*f	C_{Ex} (cm^3/s)
w_5	$1s^2\ {}^1S_0$ - $1s5p\ {}^1P_1$	3128.3	3128.1		3.307[−2]	7.344[−14]
y_5	$1s^2\ {}^1S_0$ - $1s5p\ {}^3P_1$	3129.0	3129.4		4.191[−4]	1.195[−14]
				$\Delta E_{i,j}$(eV)	F_2(i,j) (s^{-1})	C_{IS} (cm^3/s)
C_5	2s J=$\frac{1}{2}$ - $(1s2s5p_{1/2})_{1/2}$	3178.5	3177.2	2984.08	1.00[+12]	4.466[−15]
C_5	2s J=$\frac{1}{2}$ - $(1s2s5p_{3/2})_{3/2}$	3178.5	3177.3	2984.04	3.12[+12]	1.502[−14]
B_5	2s J=$\frac{1}{2}$ - $(1s2s5p_{3/2})_{1/2}$	3194.7	3192.8	2965.01	1.95[+12]	1.746[−14]
B_5	2s J=$\frac{1}{2}$ - $(1s2s5p_{3/2})_{3/2}$	3194.8	3192.9	2964.95	3.91[+12]	3.451[−14]
A_5	2p J=$\frac{3}{2}$ - $(1s2p_{3/2}5p_{1/2})_{1/2}$	3204.4	3202.0	2989.00	2.36[+12]	8.214[−15]
A_5	2p J=$\frac{1}{2}$ - $(1s2p_{1/2}5p_{3/2})_{3/2}$	3204.7	3202.4	2985.41	5.36[+12]	2.718[−14]
A_5	2p J=$\frac{3}{2}$ - $(1s2p_{3/2}5p_{3/2})_{5/2}$	3204.9	3202.5	2988.45	1.39[+13]	2.463[−14]
A_5	2p J=$\frac{3}{2}$ - $(1s2p_{3/2}5p_{3/2})_{3/2}$	3205.4	3203.1	2987.74	3.52[+12]	1.297[−14]

Table VIII. Ar^{16+} n=6 Lines with Satellites

Line	Transition	λ_{MZ} (mÅ)	λ_{Rel} (mÅ)		g*f	C_{Ex} (cm^3/s)
w_6	$1s^2\ {}^1S_0$ - $1s6p\ {}^1P_1$	3090.8	3091.1		2.086[−2]	4.035[−14]
y_6	$1s^2\ {}^1S_0$ - $1s6p\ {}^3P_1$	3091.2	3091.5		2.576[−4]	6.646[−15]
				$\Delta E_{i,j}$(eV)	F_2(i,j) (s^{-1})	C_{IS} (cm^3/s)
C_6	$2s\ J=\frac{1}{2}$ - $(1s2s6p_{3/2})_{3/2}$	3143.2	3142.1	3027.76	1.92[+12]	7.969[−15]
B_6	$2s\ J=\frac{1}{2}$ - $(1s2s6p_{3/2})_{1/2}$	3159.3	3157.5	3008.50	1.23[+12]	9.823[−15]
B_6	$2s\ J=\frac{1}{2}$ - $(1s2s6p_{3/2})_{3/2}$	3159.3	3157.5	3008.47	2.47[+12]	1.944[−14]
A_6	$2p\ J=\frac{1}{2}$ - $(1s2p_{1/2}6p_{3/2})_{3/2}$	3169.2	3167.1	3028.62	3.18[+12]	1.620[−14]
A_6	$2p\ J=\frac{3}{2}$ - $(1s2p_{3/2}6p_{3/2})_{1/2}$	3169.3	3167.2	3031.69	1.78[+12]	4.304[−15]
A_6	$2p\ J=\frac{3}{2}$ - $(1s2p_{3/2}6p_{3/2})_{5/2}$	3169.5	3167.2	3031.57	7.57[+12]	1.315[−14]
A_6	$2p\ J=\frac{3}{2}$ - $(1s2p_{3/2}6p_{3/2})_{3/2}$	3169.8	3167.5	3031.19	2.10[+12]	7.882[−15]
A_6	$2p\ J=\frac{1}{2}$ - $(1s2p_{1/2}6p_{3/2})_{3/2}$		3168.2	3027.23	8.19[+11]	6.016[−15]

Table IX. Ar^{16+} n=7 Lines with Satellites

Line	Transition	λ_{MZ} (mÅ)	λ_{Rel} (mÅ)		g*f	C_{Ex} (cm^3/s)
w_7	$1s^2\ {}^1S_0$ - $1s7p\ {}^1P_1$	3068.6	3068.9		1.724[−2]	2.456[−14]
y_7	$1s^2\ {}^1S_0$ - $1s7p\ {}^3P_1$	3068.9	3069.2		2.007[−4]	4.121[−15]
				$\Delta E_{i,j}$(eV)	F_2(i,j) (s^{-1})	C_{IS} (cm^3/s)
C_7	2s J=$\frac{1}{2}$ - $(1s2s7p_{3/2})_{3/2}$	3122.4	3121.3	3053.99	1.02[+12]	4.416[−15]
B_7	2s J=$\frac{1}{2}$ - $(1s2s7p_{3/2})_{1/2}$	3138.4	3136.6	3034.65	7.97[+11]	5.860[−15]
B_7	2s J=$\frac{1}{2}$ - $(1s2s7p_{3/2})_{3/2}$	3138.4	3136.6	3034.64	1.89[+12]	1.170[−14]
A_7	2p J=$\frac{1}{2}$ - $(1s2p_{1/2}7p_{3/2})_{3/2}$	3148.3	3146.2	3054.64	1.56[+12]	9.135[−15]
A_7	2p J=$\frac{3}{2}$ - $(1s2p_{3/2}7p_{3/2})_{5/2}$	3148.6	3146.3	3057.56	4.57[+12]	7.856[−15]
A_7	2p J=$\frac{3}{2}$ - $(1s2p_{3/2}7p_{3/2})_{3/2}$	3148.8	3146.5	3057.36	1.05[+12]	4.235[−15]

Table X. Ar^{15+} n=8-12 Satellites

Line	Transition	λ_{MZ} (mÅ)	λ_{Rel} (mÅ)	$\Delta E_{i,j}$(eV)	F_2(i,j) (s^{-1})	C_{IS} (cm^3/s)
B_8	2s J=$\frac{1}{2}$ - $(1s2s8p_{3/2})_{3/2}$	3125.0	3125.7	3048.46	1.06[+12]	7.884[−15]
A_8	2p J=$\frac{1}{2}$ - $(1s2p_{1/2}8p_{3/2})_{3/2}$	3134.9	3132.8	3071.48	9.32[+11]	6.025[−15]
A_8	2p J=$\frac{3}{2}$ - $(1s2p_{3/2}8p_{3/2})_{5/2}$	3135.2	3133.0	3074.38	3.25[+12]	5.112[−15]
A_8	2p J=$\frac{3}{2}$ - $(1s2p_{3/2}8p_{3/2})_{3/2}$	3135.3	3133.1	3074.23	7.29[+11]	3.129[−15]
A_9	2p J=$\frac{3}{2}$ - $(1s2p_{3/2}9p_{3/2})_{5/2}$	3126.1	3123.9	3085.92	2.25[+12]	3.520[−15]
A_{10}	2p J=$\frac{3}{2}$ - $(1s2p_{3/2}10p_{3/2})_{5/2}$	3119.6	3117.4	3094.16	1.63[+12]	2.520[−15]
A_{11}	2p J=$\frac{3}{2}$ - $(1s2p_{3/2}11p_{3/2})_{5/2}$	3114.8	3112.6	3100.25	1.21[+12]	1.880[−15]
A_{12}	2p J=$\frac{3}{2}$ - $(1s2p_{3/2}12p_{3/2})_{5/2}$	3111.2	3109.0	3104.88	9.22[+11]	1.427[−15]

Table XI. Calculated Ar^{16+} Rydberg Series and Measured Ar^{15+} High n Satellites

n	W_n		C_n		B_n		A_n [A'_3]	
	λ_{MZ}	λ_{Rel}	λ_{Exp}	$\Delta\lambda$	λ_{Exp}	$\Delta\lambda$	λ_{Exp}	$\Delta\lambda$
3	3365.7	3365.4	3405.7	40.3	3422.8	57.4	3427.7	62.3
							[3418.8]	[53.4]
4	3199.7	3199.6	3246.2	46.6	3262.3	62.7	3272.0	72.4
5	3128.3	3128.1	3178.4	50.3	3194.8	66.7	3204.4	76.3
6	3090.8	3091.1	3143.6	52.5	3159.3	68.2	3169.6	78.5
7	3068.6	3068.9	3122.1	53.2	3138.6	69.7	3148.4	79.5
8	3054.4	3054.8			3125.6	70.8	3135.0	80.2
9	3044.7	3045.1					3125.6	80.5
10	3037.8	3038.2					3119.4	81.2
11	3032.8	3033.1					3115.3	82.2
12	3028.9	3029.2					3111.0	81.8
13	3025.9	3026.3						

Table XII. Calculated S^{14+} w_n Rydberg Series

n	λ_{MZ} (mÅ)	λ_{Rel} (mÅ)	A_{ij} (s^{-1})	g*f
3		4299.4		.1634
4	4088.5	4088.9	7.28[12]	.0637
5	3997.7	3998.2	3.63[12]	.0324
6	3950.1	3950.5	2.07[12]	.0192
7	3921.9	3922.4	1.29[12]	.0126
8	3903.8	3904.3	8.60[11]	.0090
9	3891.5	3892.0	6.02[11]	.0069
10	3882.8	3883.3	4.38[11]	.0056
11	3876.3	3876.8	3.28[11]	.0049
12	3871.5	3871.9	2.52[11]	.0050
13	3867.7	3868.1	1.98[11]	.0074

Table XIII. Calculated S^{13+} 2p J=$\frac{3}{2}$ - $(1s2p_{3/2}np_{3/2})_{5/2}$ Series

n	λ_{MZ} (mÅ)	λ_{Rel} (mÅ)	$F_{2,MZ}$ (s^{-1})	$F_{2,Rel}$ (s^{-1})	$\Delta E_{i,j}$ (eV)	C_{IS} (cm^3/s)
3	4388.6	4386.5	5.52[+13]	5.21[+13]	2149.50	7.867[−14]
4	4193.0	4189.0	1.82[+13]	1.72[+13]	2282.78	1.699[−14]
5	4108.1	4104.4	1.03[+13]	1.04[+13]	2343.79	9.056[−15]
6	4063.6	4060.0	6.02[+12]	5.87[+12]	2376.79	4.750[−15]
7	4037.3	4033.7	3.66[+12]	3.58[+12]	2396.73	2.895[−15]
8	4020.4	4016.8	2.39[+12]	2.34[+12]	2409.62	1.924[−15]
9	4008.9	4005.4	1.65[+12]	1.62[+12]	2418.45	1.315[−15]
10	4000.7	3997.2	1.19[+12]	1.16[+12]	2424.77	9.402[−16]